Geophysical Journal International

Geophys. J. Int. (2024) **240,** 1028–1047
Advance Access publication 2024 November 29
GJI Seismology

https://doi.org/10.1093/gji/ggae426

Estimation of source characteristics, site effects and path attenuation in the Sichuan Basin, China, using a non-parametric generalized inversion technique

Pengfei Dang [1,2,3] Jie Cui,[2] Hongfeng Yang [3,4] and Jian Song[5]

[1]*School of Civil and Environmental Engineering and Geography Science, Ningbo University, Ningbo* 315211, *China. E-mail: iempengfeid@qq.com*
[2]*School of Civil Engineering and Transportation, Guangzhou University, Guangzhou* 510006, *China.*
[3]*Department of Earth and Environmental Sciences, Faculty of Science, The Chinese University of Hong Kong, Shatin, NT, Hong Kong* 999077, *China.*
[4]*Shenzhen Research Institute, The Chinese University of Hong Kong, Shenzhen, Guangdong* 518172, *China.*
[5]*Guangdong Hualu Transportation Technology Co., Ltd, Guangzhou* 510550, *China.*

Accepted 2024 November 26. Received 2024 October 29; in original form 2023 September 11

SUMMARY

A non-parametric generalized inversion technique for the *S*-wave amplitude spectrum on both the horizontal and vertical components was adopted to calculate the source parameters, site effects and path attenuations. In this scheme, 1647 three-component records corresponding to 78 earthquakes with M_s values of 2.9–6.0 recorded by 58 strong-motion stations in the Sichuan Basin were used. In the non-parametric generalized inversion technique, a reference station was adopted to remove the trade-off between the site and source terms. Then, the simple model $R^{-0.5}$ was selected to describe the geometric spreading characteristics of the Sichuan Basin region. The frequency-related quality factor models for the horizontal and vertical components are estimated as $Q(f) = 129.9872f^{1.1119}$ and $Q(f) = 132.54f^{1.1236}$, respectively. In addition, the inverted source spectra are well matched with Brune's model, in which the stress drop values range between 0.3 and 3.5 MPa with a mean value of 1.36 MPa. In addition, a comparison between the site effects estimated from horizontal-to-vertical and non-parametric generalized inversion methods shows that the geological environment significantly amplifies the vertical component of ground motion. Finally, a residual related to distance and magnitude indicates that there is no obvious dependence of the scatter on distance or magnitude. The source, path and site parameters estimated in this inversion can be adopted in ground motion simulations, which could aid in the study of seismic disasters and risk assessment in the Sichuan Basin.

Key words: Earthquake ground motions; Earthquake source observations; Seismic attenuation; Site effects; Wave propagation.

1. INTRODUCTION

The Sichuan Basin is an intracontinental basin located in central China containing semiconsolidated sediments from the Paleozoic, Mesozoic and Cenozoic eras, as well as sedimentary rocks with a thickness of several kilometres (Guo *et al.* 2023). In the past decade, many medium-sized earthquakes have been reported in the Sichuan Basin and its surrounding regions, such as the M_s 6.0 Changning earthquake in 2019, the M_s 5.6 Gongxian earthquake in 2019 and the M_s 5.4 Lushan earthquake in 2013. Although the earthquakes occurring in this seismogenic area are mainly small and medium-sized, the likelihood of large and destructive earthquakes remains relatively high. Therefore, the evaluation of seismic hazards and the formulation of an event mitigation strategy in the Sichuan Basin are critical tasks (Zhou *et al.* 2022). Seismic hazard assessment may benefit from a gradual understanding of the observed ground motions. Moreover, earthquake ground motions and the resulting damage depend on path attenuation from medium characteristics and local site effects (Jeong *et al.* 2020). Previous studies have suggested complex path attenuation and strong site effects in the Sichuan area (Wang *et al.* 2018; Fu *et al.* 2019; Zhang *et al.* 2023).

Accurately predicting earthquake ground motion is an effective method for the seismic design of building structures and reducing earthquake disasters. By analysing the characteristics of observed records, the specific effects of the source, propagation path and near-surface site conditions on ground motion can be determined, providing an important basis for ground motion simulation and the establishment of ground motion prediction equations (Boore, 2003; Kale *et al.* 2015; Wang *et al.* 2017). The generalized inver-

sion technique (GIT) was first developed for effectively dividing the source, path and site items in ground motion in the frequency domain (Andrews 1986). Many studies have focused on seismic hazard analysis, ground motion parameter prediction and ground motion simulation (Parolai *et al.* 2000; Shoji & Kamiyama 2002; Hassani *et al.* 2011; Mandal & Dutta 2011; Zafarani *et al*., 2012; Grendas *et al.* 2018; Klin *et al.* 2018; Fernández *et al.* 2022). The GIT has been an effective tool for estimating the source parameters, regional quality factors and site responses of small and medium-sized earthquakes. Unfortunately, in the GIT, a highly specific geometric spreading function and functional shape of the quality factor are used to describe the influence of the seismic wave propagation path on ground motion. Due to the non-uniformity and anisotropy of the Earth's internal media, there is uncertainty when describing the attenuation characteristics of seismic waves in propagation media. Moreover, the uncertainty of attenuation characteristics often leads to abnormally high or even negative quality factors in some frequency bands, resulting in deviations in the source spectrum or site amplification (Castro *et al.* 1990; Salazar *et al.* 2007). To solve this problem, the non-parametric generalized inversion technique (NONGIT) was proposed (Castro *et al.* 1990), in which a discrete variable that only depends on distance is defined to describe the attenuation characteristics of seismic waves of different frequencies in the propagation medium, and this variable follows two basic assumptions: (1) at the reference distance, there is no path attenuation of seismic waves, and (2) this variable is a monotonically decreasing curve of distance (Wang *et al.* 2017; Jeong *et al.* 2020). To date, there has been relatively little research on site effects and path attenuation in the Sichuan Basin, and most of the research results are based on seismic data. Although Wang *et al.* (2018) conducted research on the source characteristics, path attenuation and site effects of the Wenchuan area using a non-parametric generalized inversion technique based on strong-motion data, the data selected were only from aftershocks of the 2008 M_w 7.9 Wenchuan earthquake.

Based on the observed ground-motion data sets in the Sichuan Basin area from 2009 to 2021, spectral decomposition was performed to simultaneously divide the source, path and components in the frequency domain (Jeong *et al.* 2020). The path attenuation functions, including the geometric propagation and anelastic attenuation functions, were first systematically analysed. The source spectra of 78 earthquake events were reliably determined from the estimated source spectra and then adopted to investigate the source features in the Sichuan Basin. The study of path attenuation functions and source features is essential for the interpretation of damage and earthquake physics, the reliable prediction of ground motion and the assessment of seismic hazards (Wang *et al.* 2018).

2. DATA PROCESSING

We collected 4449 well-recorded three-component earthquake records from 165 earthquake events, recorded at 174 strong-motion stations in the Sichuan Basin from 2009 to 2021. These records were provided by the China Strong Motion Network Centre (CSMNC) and cover acceleration records from the 2019 M_s 5.1 Rongxian earthquake, 2011 M_s 3.9 Maoxian earthquake, 2013 M_s 4.5 Lushan earthquake, 2014 M_s 4.9 Lixian earthquake and 2016 M_s 4.5 Beichuan earthquake (Fig. 1). Some strong-motion acceleration records from the CSMNC provide surface wave magnitudes (M_s), while some records are local magnitudes (M_L). In our study, we converted M_L into M_s (Wang *et al.* 2010) and M_s was subsequently adopted to represent the value measured by the CSMNC. Most of the records are related to $M_s < 6.0$ events, and most of the earthquakes occurred on the edge of the Sichuan Basin. These records have a sample rate of 200 Hz. By comparing two normalized spectra recorded at hypocentral distances of 4 and 62 km, Jeong *et al.* (2020) concluded that when the frequency is greater than 25 Hz, the attenuation of the *S*-wave may not fully describe the path and site effects. Therefore, in this inversion, the cutoff frequency is set to 25 Hz. To compute the Fourier amplitude spectrum (FAS) of the acceleration histories, the following procedure was used. First, the acceleration recordings were filtered using a fourth-order Butterworth filter after baseline correction. The *S*-wave amplitude spectra of the horizontal components were then obtained based on the method provided by Husid (1967) and McCann (1979). The starting point of the *S*-wave was defined as the abruptly increasing point in the Husid plot, and we chose the end time of the *S*-wave window where the cumulative envelope function started to decrease to shut the coda wave out (Sadeghi-Bagherabadi *et al.* 2020; Dang et al. 2023). In this study, the ending point of the background noise window was determined to be 2.0 s before the onset of the *P* wave. A 10 per cent Hanning window was applied at both ends of the *S* wave to eliminate truncation errors (Hassani *et al.* 2011; Ren *et al.* 2018; Wang *et al.* 2018; Wang *et al.* 2019; Wang & Wen 2020). After data processing, the *S* wave can be extracted (Fig. 2). Individual records were selected by visual inspection of seismograms with an average signal-to-noise ratio (SNR) greater than 5 (Mandal & Dutta 2011; Jeong *et al.* 2020), and at each frequency point, only recordings with an SNR greater than 5 were retained (Fig. 3). The low-cut corner frequency f_{lc} was defined by the SNR and was set to 0.25 Hz (Zhou *et al.* 2022; Dang *et al.* 2024). Due to sudden changes in the FAS, the signals must be smoothed by the windowing function with parameter $b = 20$ (Konno & Ohmachi, 1998):

$$W(f, f_c) = \left[\frac{\sin\left[\log\left(f/f_c\right)^b\right]}{\log\left(f/f_c\right)^b} \right]^4, \quad (1)$$

where f_c indicates the central frequency.

In this study, the root-mean-square (i.e. $\sqrt{(EW^2 + NS^2)/2}$) of the two horizontal FAS values was defined as the horizontal amplitude of ground motion of the *S* wave in the frequency domain (Fig. 4).

In this study, the available records were selected from the data set according to the following criteria given by Wang *et al.* (2018). First, recordings with hypocentral distances between 10 and 80 km were selected. Within this distance range, the data distribution is relatively dense, which can reduce the degree of dispersion and increase the stability of the inversion results. Then, the average peak ground accelerations (PGAs) in both the horizontal and vertical components ranging from 2 to 100 cm s^{-2} were selected to reduce the impact of background noise and the non-linear response of the soil layer on the site. Finally, an earthquake event should be recorded by at least four strong-motion stations, with each station triggered by at least four earthquakes to reduce data discreteness and ensure inversion algorithm stability. Because the Wenchuan aftershocks from 2008 to 2013 were used to estimate the source parameters, path attenuation and site effects, relevant data were removed from this study. Therefore, a total of 1647 three-component strong-motion recordings collected at 58 stations for 78

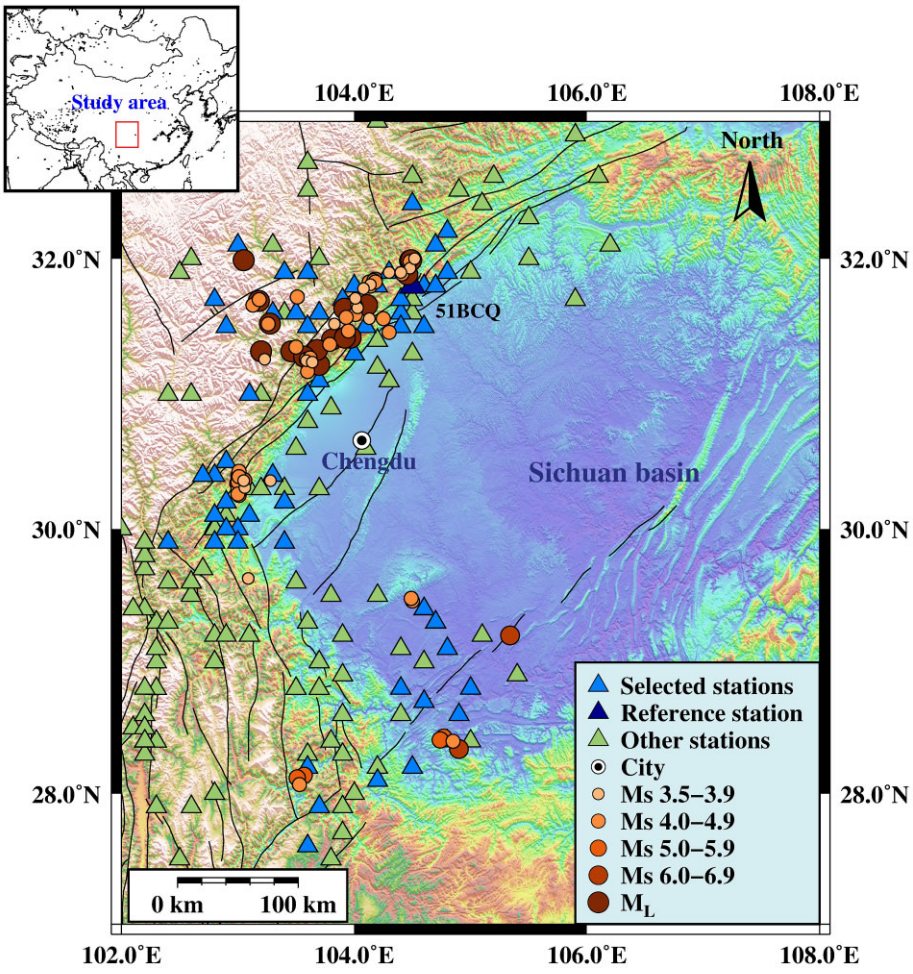

Figure 1. The distributions of selected earthquake events (circles) and strong-motion stations (triangles) used in our scheme. The thin solid lines indicate faults, and the triangles denote strong motion stations. The inset map indicates the location of the study area.

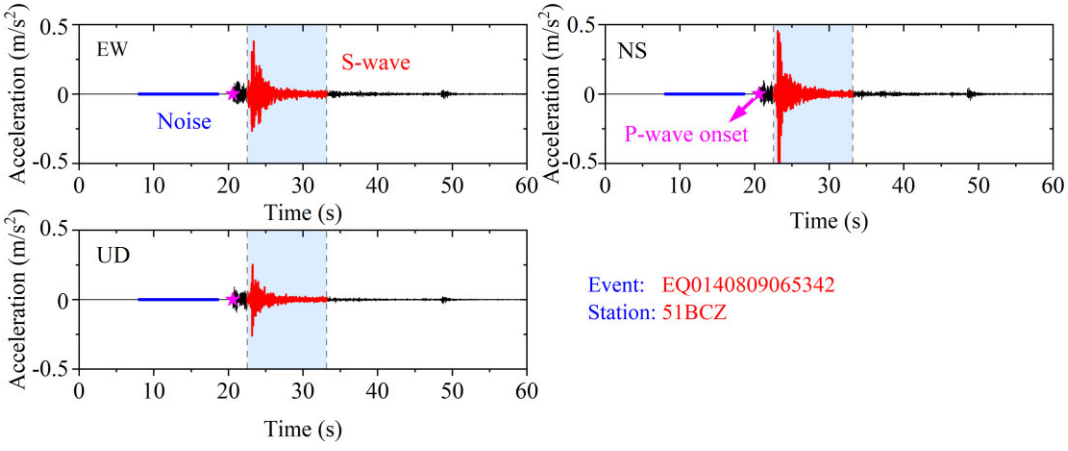

Figure 2. Three-component accelerations for the EQ0140809065342 event recorded at station 51BCZ.

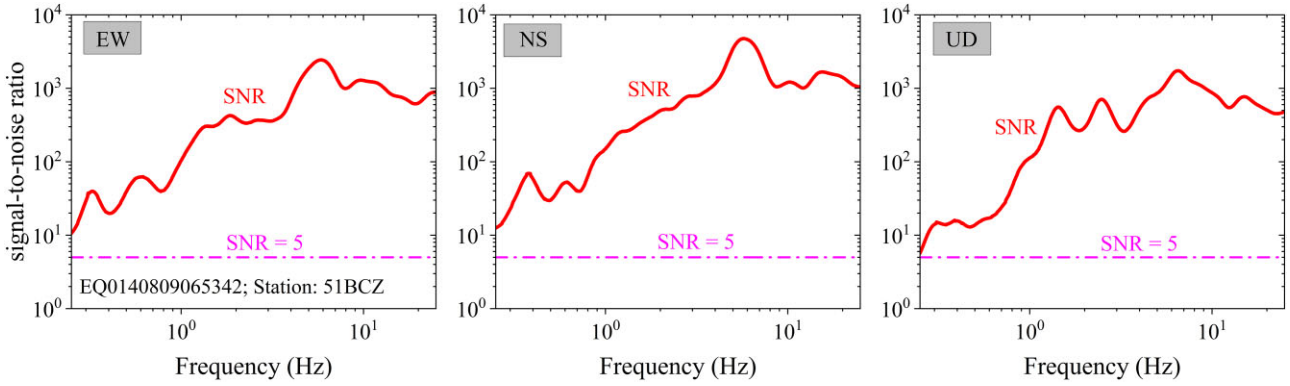

Figure 3. SNR for the EQ0140809065342 event recorded at the 51BCZ station. The SNR at each frequency is shown by a solid line.

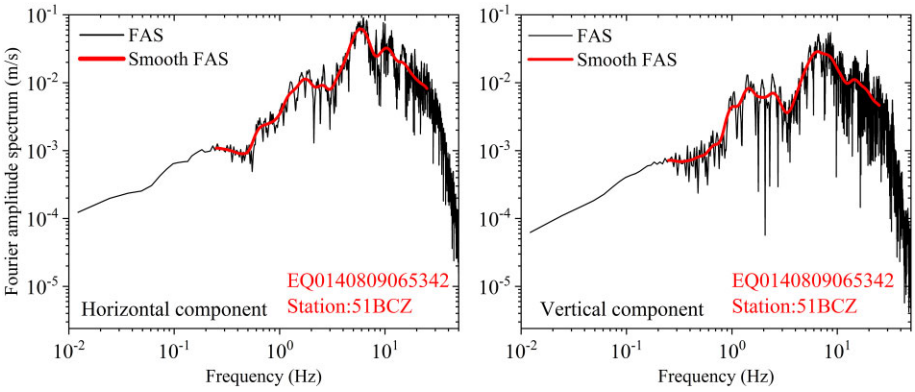

Figure 4. The FAS and smoothed FAS for the EQ0140809065342 event recorded at the 51BCZ station.

Ms 2.9–6.0 earthquakes from 2011 January 16 to 2021 September 16, were included in this inversion (Table 1). Among these 78 earthquakes, 32 had magnitudes (M_s) less than 4.0, 37 had M_s values between 4.0 and 4.9, and 9 had magnitudes greater than 5.0. The depth of the seismic source is mainly concentrated within the range of 10–20 km, and the M_s values in the range of 2.9 to 6.0 and hypocentral distances from 10 to 80 km were analysed (Fig. 5).

3. GENERALIZED INVERSION METHOD

3.1 Parametric generalized inversion technique

The GIT was applied to divide frequency-related path attenuations, site effects and source characteristics in the recorded FAS in the frequency domain:

$$U_{ij}(f, R_{ij}) = S_i(f) \cdot A(f, R_{ij}) \cdot G_j(f), \tag{2}$$

where $U_{ij}(f, R_{ij})$, $S_i(f)$, $A(f, R_{ij})$ and $G_j(f)$ denote the FAS from the ith source and the jth strong-motion station at the hypocentral distance R, the source function, the attenuation function along the path and the local amplification of the site, respectively.

When using the GIT, the attenuation function $A(f, R_{ij})$ can be divided into the geometric spreading function $GS(R_{ij})$ and inelastic attenuation $\exp(-\pi f R_{ij}/Q(f)\beta)$, in which $Q(f)$ and β ($= 3.6\ \mathrm{km\ s^{-1}}$) denote the quality factor and S-wave velocity near the source, respectively.

By taking natural logarithms on both sides, the following linear form is obtained:

$$\ln U_{ij}(f) - \ln GS(R_{ij}) + \pi f R_{ij} \big/ Q(f)\beta = \ln S_i(f) + \ln G_j(f). \tag{3}$$

If the data sets have M recordings, eq. (3) can be transformed into a linear system of equations $\mathbf{A}\boldsymbol{x} = \boldsymbol{b}$, in which $\mathbf{A}$, $\boldsymbol{x}$ and $\boldsymbol{b}$ denote the system matrix related to the data and model vectors, the vector containing the model parameters and the data vector consisting of the logarithmic spectral amplitudes, respectively. Andrews (1986) reported the existence of an undetermined degree of freedom between source and site components. This uncertain degree of freedom can either be removed by selecting a reference site or one (or several) source spectra. Then, the vector containing the unknown source, path and site components can be obtained by the singular value decomposition (SVD) algorithm proposed by Menke (1989).

3.2 Non-parametric generalized inversion technique

The non-parametric GIT algorithm, which was originally proposed by Castro *et al.* (1990), was applied to divide the FAS algorithm into source, path and site components. In our scheme, the modified version was used. In the non-parametric GIT, eq. (2) can be written in linear form by simply applying logarithms (Jeong *et al.* 2020):

$$\log U_{ij}(f, R_{ij}) = \log S_i(f) + \log A(f, R_{ij}) + \log G_j(f). \tag{4}$$

Table 1. The station ID, station code, geographic coordinates, site conditions and number of recordings of selected stations.

Station ID	Station code	Latitude	Longitude	Number of records	Site condition
1	51ZGS	29.4	104.6	3	Rock
2	**51BCZ**	31.9	104.3	11	Soil
3	53YST	28.2	103.6	2	Soil
4	**51BCB**	31.8	104.2	18	Soil
5	***51BCQ***	*31.8*	*104.5*	*13*	*Rock*
6	**51AXD**	31.6	104.4	10	Soil
7	**51MZX**	31.5	104.1	10	Soil
8	**51MXF**	31.8	104	25	Soil
9	**51DJH**	31.1	103.7	9	Soil
10	**51LXK**	31.6	103.3	18	Soil
11	**51BXY**	30.5	102.9	11	Soil
12	**51BXZ**	30.5	102.9	5	Soil
13	**51LXT**	31.6	103.5	33	Soil
14	**51MZQ**	31.5	104.1	11	Soil
15	**51BCY**	31.7	104.4	11	Soil
16	**51BXD**	30.4	102.8	12	Soil
17	**51JYH**	31.8	104.6	7	Soil
18	**51DJZ**	31	103.6	6	Soil
19	**51QLY**	30.4	103.3	7	Soil
20	51CNT	28.6	104.9	3	Rock
21	**51PWP**	32.1	104.7	9	Soil
22	**51YAM**	30.1	103.1	12	Soil
23	**51LSJ**	30.2	102.9	5	Soil
24	51ZG1	29.3	104.7	3	Soil
25	51ZG3	29.3	104.7	3	Rock
26	53YSZ	27.9	103.7	3	Soil
27	**51MXN**	31.6	103.7	30	Soil
28	**51WCD**	31.5	103.6	19	Soil
29	**51MXB**	31.9	103.6	22	Soil
30	**51SFB**	31.3	104	21	Soil
31	**51JYW**	31.8	104.7	8	Soil
32	**51AXH**	31.5	104.6	6	Soil
33	**51MXD**	31.7	103.9	8	Soil
34	**51LXS**	31.5	102.9	9	Soil
35	**51TQD**	30.1	102.8	6	Soil
36	**51BXM**	30.4	102.7	9	Soil
37	**51YAD**	30	103	10	Soil
38	51JLD	28.2	104.5	5	Rock
39	**51LSF**	30	102.9	7	Soil
40	51YBT	28.7	104.6	4	Soil
41	**51PWN**	32.2	104.8	5	Soil
42	**51JYC**	31.9	104.8	5	Soil
43	**51HSS**	31.9	103.4	14	Soil
44	**51WCW**	31	103.1	13	Soil
45	**51PJD**	30.2	103.4	8	Soil
46	**51YAS**	29.9	103	11	Soil
47	**51LXM**	31.7	102.8	8	Soil
48	**51AXT**	31.5	104.4	5	Soil
49	**51PWD**	32.4	104.5	8	Soil
50	**51YAL**	29.9	102.8	11	Soil
51	51NXT	28.8	105	3	Soil
52	**51HYT**	29.9	103.4	7	Soil
53	51FSB	29.1	104.8	5	Rock
54	**51HSD**	32.1	103	5	Soil
55	53YML	27.6	103.6	3	Soil
56	51YBG	28.8	104.4	5	Soil
57	53YJT	28.1	104.2	3	Rock
58	**51TQL**	29.9	102.4	6	Soil

Unit: Latitude, °; Longitude, °; The site conditions are as indicated in the headlines of raw acceleration files. The italic-row character indicates the selected reference station. The number of records represents the number of records for a single component. The bold characters represent the data set used for non-parametric GIT.

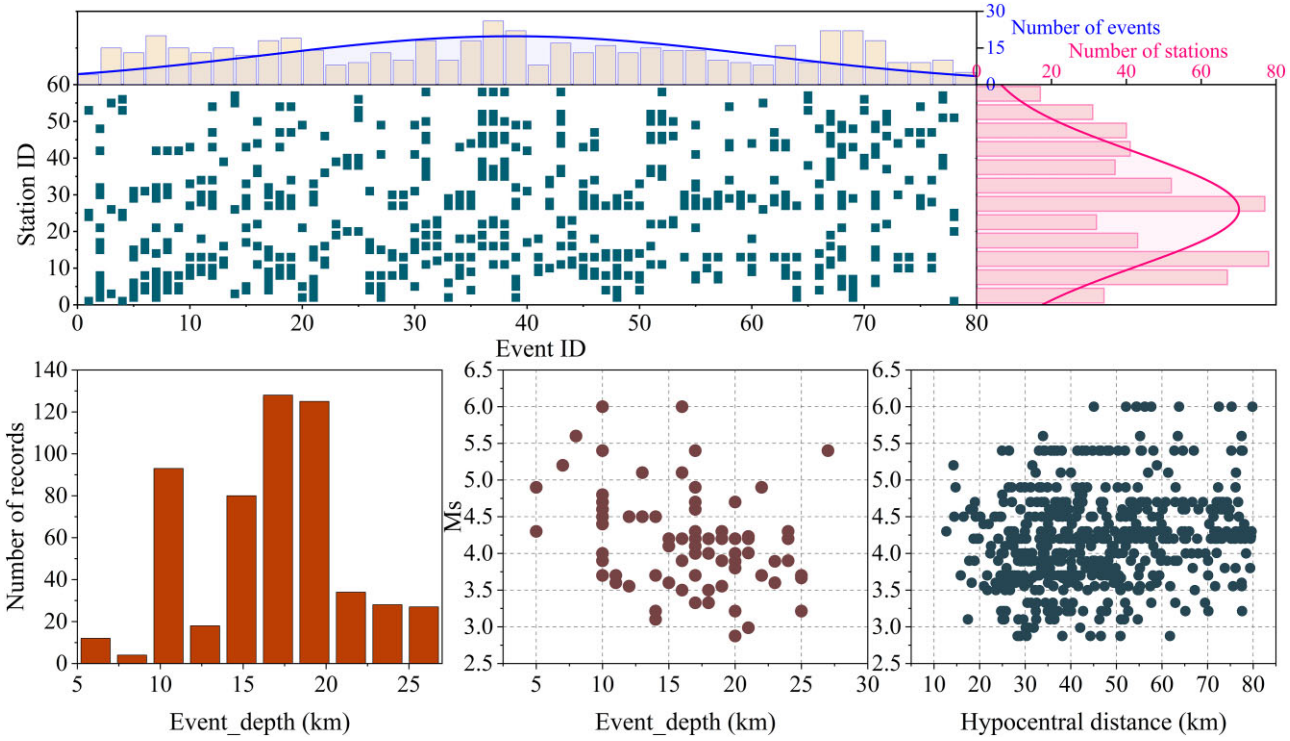

Figure 5. Data sets adopted in our scheme. *Top panel*: distribution of event recordings divided for the different strong-motion sites. *Bottom panel*: distribution of the number of records with event depth in km (left), distribution of surface wave magnitude (M_S) with event depth in km (middle), and distribution of M_S with hypocentral distance in km (right). Some M_S are measured by the China Earthquake Network Center, while some are converted from the local magnitude M_L.

In our scheme, the matrix $\mathbf{A}\boldsymbol{x} = \boldsymbol{b}$ can be written as follows (Jeong *et al.* 2020):

$$\left[\begin{array}{ccccc|c|c}
1 & 0 & 0 & \cdot & \cdots & 1\ 0\ 0\ \cdots & 1\ 0\ 0\ \cdots \\
0 & 1 & 0 & \cdot & \cdots & 1\ 0\ 0\ \cdots & 1\ 0\ 0\ \cdots \\
\cdot & \cdot & \cdot & \cdot & \cdots & \cdot\ \cdot\ \cdot\ \cdots & \cdot\ \cdot\ \cdot\ \cdots \\
1 & 0 & 0 & \cdot & \cdots & 0\ 1\ 0\ \cdots & 0\ 1\ 0\ \cdots \\
\vdots & \vdots & \vdots & \vdots & \vdots & \vdots\ \vdots\ \vdots\ \cdots & \vdots\ \vdots\ \vdots\ \cdots \\
\omega_1 & 0 & 0 & \cdot & \cdots & 0\ 0\ 0\ \cdots & \cdot\ \cdot\ \cdot\ \cdots \\
0 & 0 & 0 & \cdot & \cdots & \omega_3\ 0\ 0\ \cdots & \cdot\ \cdot\ \cdot\ \cdots \\
-\omega_2/2 & \omega_2 & -\omega_2/2 & 0 & \cdots & 0\ 0\ 0\ \cdots & \cdot\ \cdot\ \cdot\ \cdots \\
0 & -\omega_2/2 & \omega_2 & -\omega_2/2 & \cdots & \cdot\ \cdot\ \cdot\ \cdots & \cdot\ \cdot\ \cdot\ \cdots \\
\cdot & \cdot & \cdot & \cdot & \cdots & \cdot\ \cdot\ \cdot\ \cdots & \cdot\ \cdot\ \cdot\ \cdots
\end{array}\right]$$

$$\times \begin{bmatrix} \log A_1 \\ \cdot \\ \cdot \\ \log A_{M1} \\ \log G_1 \\ \cdot \\ \cdot \\ \log G_{M2} \\ \log S_1 \\ \cdot \\ \cdot \\ \log S_{M3} \end{bmatrix} = \begin{bmatrix} \log U_{11} \\ \cdot \\ \cdot \\ \log U_{ij} \\ \vdots \\ 0 \\ 0 \\ 0 \\ 0 \\ \cdot \end{bmatrix} \tag{5}$$

In eq. (5), ω_1 denotes the weighted parameter used to constrain the amplitude level, making logA(f, R_0) equal to 0, in which R_0 denotes the reference distance, which can be defined as the minimum hypocentral distance of 13 km in this inversion. In addition, the attenuation operator is written as a non-parametric function of the binned distance. ω_2 denotes the degree of smoothness and ω_3 represents the weight applied to resolve the undermined degree of freedom between the site and source components. $M1$, $M2$ and $M3$ indicate the number of distance intervals, stations and earthquakes, respectively. (Andrews 1986; Jeong *et al.* 2020).

It has long been recognized that acceleration amplitudes above a threshold frequency decay sharply due to local site effects (Hanks 1982; Sadeghi-Bagherabadi *et al.* 2020). A κ parameter was introduced to quantify this near-surface attenuation (Anderson & Hough 1984). Papageorgious & Aki (1983) suggested that the seismic source effect is the main reason for the attenuation of the seismic amplitude spectrum in the high-frequency range. Anderson & Hough (1984) suggested that the κ parameter is influenced mainly by the geological structure near the surface and has a certain relationship with the epicentral distance. There are also studies indicating that the main reasons for the attenuation of the amplitude spectrum in the high-frequency range are the seismic source and near-surface attenuation effects, which have a small dependence on the propagation path (Tsai & Chen 2000). According to Campbell (2009), the attenuation characteristics of seismic motion are influenced mainly by geological conditions near the surface and the effects of seismic sources. Although different scholars have different physical interpretations of the κ parameter, it is generally believed that the κ parameter is related to the near-surface geological conditions of the site. In this study, the high-frequency spectral decay parameter kappa (κ_0) was set to 0.047 s for the basin area (Fu *et al.* 2019), which was higher than the average kappa value of 0.0319 s for the mountain areas in Sichuan and slightly smaller than the average kappa value of 0.0475 s estimated for the Sichuan basin area (Guo *et al.* 2023). This may be because of the surficial soil layers where the stations are located (Askan *et al.* 2014; Fu *et al.* 2019).

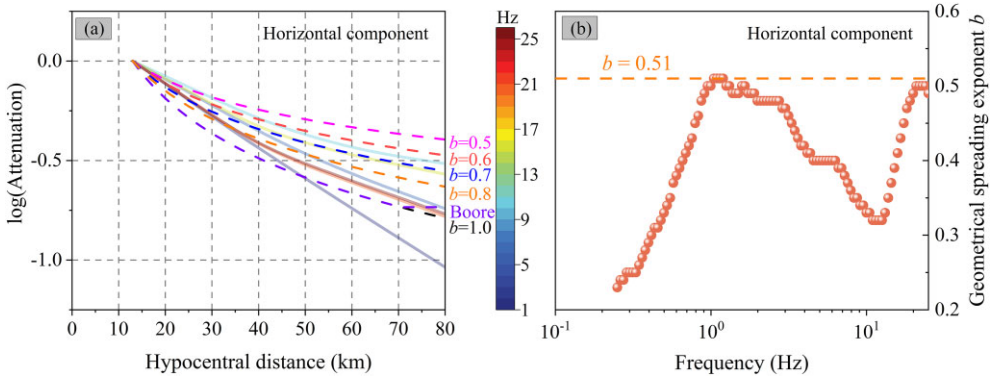

Figure 6. (a) Non-parametric attenuation functions versus the hypocentral distance at frequency points of 1, 6, 10, 15, 20 and 25 Hz in horizontal component. $R^{-0.5}$, $R^{-0.6}$, $R^{-0.7}$ $R^{-0.8}$, R^{-1} and the three-stage geometric spreading function defined by Boore (2003) are represented by the dashed lines. (b) The geometrical spreading exponent b (vertical component) for all selected frequencies.

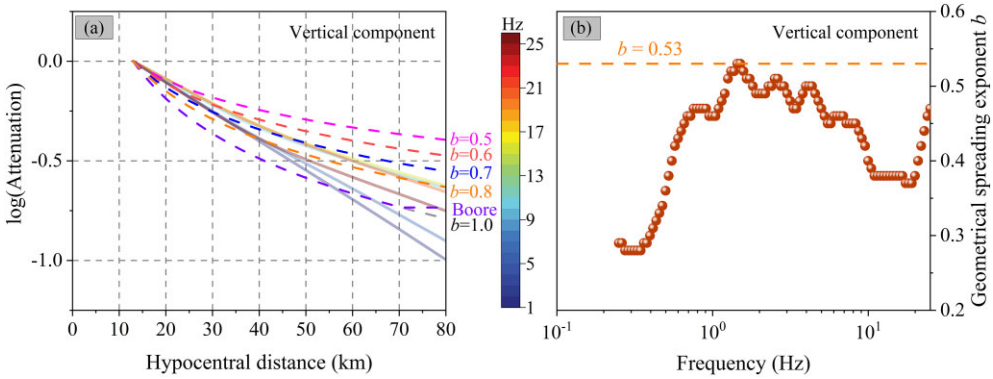

Figure 7. (a) Non-parametric attenuation functions versus the hypocentral distance at frequency points of 1, 6, 10, 15, 20 and 25 Hz in vertical component. $R^{-0.5}$, $R^{-0.6}$, $R^{-0.7}$ $R^{-0.8}$, R^{-1} and the three-stage geometric spreading function defined by Boore (2003) are represented by the dashed lines. (b) The geometrical spreading exponent b (vertical component) for all selected frequencies.

4. RESULTS AND DISCUSSION

In our scheme, the horizontal and vertical decay functions were obtained from the non-parametric GIT. By comparing the non-parametric spectral attenuations and widely used geometric spreading functions, the path attenuation was analysed and the optimal geometric attenuation function was determined. Afterwards, the best-fitting quality factor model for the Sichuan Basin could be obtained by the inverted model. To ensure the reliability of the inversion results, in this study, 50 bootstrap analyses provided by Parolai *et al.* (2000, 2004) were performed at each frequency point, and finally, the average path attenuation, site effect and source spectra were obtained.

4.1 Spectral attenuation

The non-parametric spectral attenuation is defined as a function of the geometric spreading function and anelastic attenuation, which can be written as follows:

$$A(f, R) = \left(\frac{R_0}{R}\right)^b \exp\left[\frac{-\pi f}{\beta Q(f)}(R - R_0)\right], \quad (6)$$

where f, R and b denote the frequency (Hz), the hypocentral distance (km) and the geometrical spreading exponent, respectively. R_0 represents the reference distance, β represents the S-wave velocity (km s^{-1}) and $Q(f)$ accounts for the quality factor in terms of $Q(f) = Q_0 f^{\eta}$, in which η is the index.

Because there is a strong trade-off between the geometric spreading exponent b and the frequency-related quality factor $Q(f)$, the generally used geometric spreading function (R^{-1}) is not suitable for the Sichuan Basin region (Figs 6a and 7a). In the parametric GIT, we usually estimate $Q(f)$ by determining the geometric spreading in advance, such as $b = 1$. However, in the non-parametric GIT, we obtained non-parametric attenuation functions by solving eq. (5). To define the non-parametric path attenuation as a function related to distance, it is necessary to divide the distance range, such as 13–80 km in this inversion, into multiple bins and ensure that there is a certain amount of data in each bin. If the selected bins are set too large, the smoothing constraint will suppress spatial changes and result in inappropriate spectral attenuation functions (Ameri *et al.* 2011). Because the hypocentral distance of the selected recordings in this study is uniformly distributed with local magnitude (Fig. 5), a fixed bin width, such as 1 km, was selected to calculate the non-parametric attenuation functions.

By taking the natural logarithms of both sides of eq. (6), we obtain:

$$\ln A(f, R) - \ln\left(\frac{R_0}{R}\right)^b = \frac{-\pi f}{Q(f)\beta}(R - R_0). \quad (7)$$

Considering that the difference between $\ln A(f, R)$ and $\ln(R_0/R)^b$ should be less than zero, which means that $\ln A(f, R) - \ln(R_0/R)^b < 0$ (Wang *et al.* 2018; Sakhaei *et al.* 2022), we obtained the maximum value of exponent b at each frequency point for both the horizontal and vertical components, as shown in Figs 6(b) and 7(b), which is

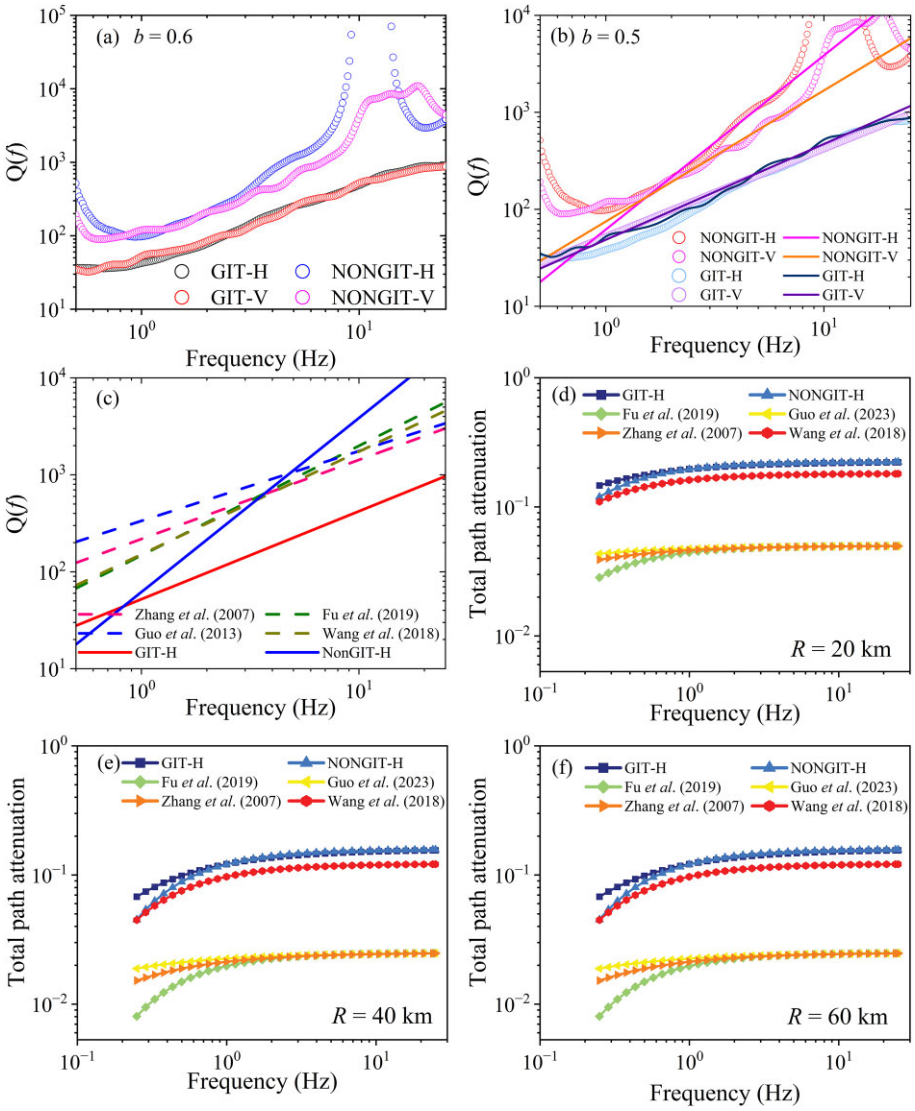

Figure 8. Comparison of the total path attenuation and quality factor obtained from different models. (a) The inverted quality factors estimated with geometrical spreading exponent $b = 0.6$. The inverted quality factors obtained from GIT-H, GIT-V, NONGIT-H and NONGIT-V are represented by circles. (b) The inverted quality factors (circles) and the best-fitting Q-models (solid lines) in this study with geometrical spreading exponent $b = 0.5$. The best-fitting Q-models inverted by GIT-H, GIT-V, NONGIT-H, and NONGIT-V are represented by the solid lines. (c) Comparison of quality factor models between this study and previous studies. The solid lines represent the Q-models for the horizontal (NONGIT-H; GIT-H) component and the other dotted lines represent the Q-models given by previous studies. (d)–(f) Comparison of total path attenuations with hypocentral distances of 20, 40 and 60 km.

Table 2. Some of the Q models and related geometrical spreading functions compared in this study.

No.	Q model	GSF	Region	References
1	$Q(f)=132.3729f^{0.8409}$	$R^{-0.5}$	Sichuan Basin, China	This study (GIT-H)
2	$Q(f)=138.0317f^{0.901}$	$R^{-0.5}$	Sichuan Basin, China	This study (GIT-V)
3	$Q(f)=129.9872f^{1.1119}$	$R^{-0.5}$	Sichuan Basin, China	This study (NONGIT-H)
4	$Q(f)=132.54f^{1.1236}$	$R^{-0.5}$	Sichuan Basin, China	This study (NONGIT-V)
5	$Q(f)=147.5f^{1.13}$	R^{-1}	Sichuan Basin, China	Fu *et al.* (2019)
6	$Q(f)=335.0f^{0.72}$	R^{-1}	Sichuan Basin, China	Guo *et al.* (2023)
7	$Q(f)=217.8f^{0.816}$	R^{-1}	Sichuan Basin, China	Zhang *et al.* (2017)
8	$Q(f)=151.2f^{1.06}$	$R^{-0.57}$	Wenchuan, China	Wang *et al.* (2018)

Note: GSF: related geometrical spreading function.

also considered the strongest geometric spreading function (Wang *et al.* 2018; Sakhaei *et al.* 2022). In this case, the *S*-wave quality factor model $Q(f)$ can be obtained from the slope of a linear least-squares fit of eq. (7) at each frequency.

In our scheme, we obtained non-parametric path attenuation functions via the non-parametric GIT. The estimated non-parametric path attenuations of the *S* wave for the horizontal and vertical components are plotted in Figs 6 and 7. The results indicate that the

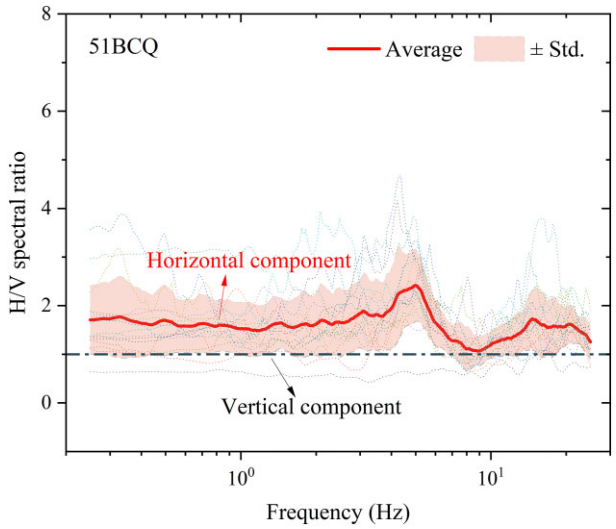

Figure 9. Average H/V spectral ratio (solid line) for station 51BCQ, showing nearly unity for the 0.25–25 Hz frequency band. The dashed line indicates the unit site amplification, and the shaded area represents the ± standard deviation.

path attenuation decays significantly with distance when the distance is less than 45 km, while at larger distances, the attenuation is slow and gradually tends to plateau. In addition, the path attenuation of *S* waves for both horizontal and vertical components with higher frequencies showed a decreasing attenuation compared to lower frequencies. In general, attenuation functions monotonically decay with increasing frequency (Ameri *et al.* 2011; Ahmadzadeh *et al.* 2017; Sakhaei *et al.* 2022). However, compared to those at low frequencies, the attenuation functions of the horizontal and vertical components obtained in this study exhibit decreased decay at high frequencies (Jeong *et al.* 2020). These results are consistent with the path attenuation characteristics of the Fort Worth Basin in Texas calculated by the non-parametric GIT (Jeong *et al.* 2020). As stated in previous research, the path effect should be the primary factor contributing to differences in the shapes of the two spectra. This indicates that the attenuation of seismic waves in the Sichuan Basin is particularly complex. Because most of the observation stations selected in this inversion are located on the northwest edge of the Sichuan Basin, the Moho depth in this area varies from 52.5 km in the northwest to 41.5 km in the southeast (Chen & Xu, 2013).

Fig. 6(b) indicates that the geometric attenuation of the horizontal component in the Sichuan Basin gradually increases with increasing frequency at low frequencies, decreases with increasing frequency at frequencies less than 10 Hz and finally increases until reaching 20 Hz. This attenuation characteristic is basically consistent with that given by Wang *et al.* (2018) in the Wenchuan area. However, the geometric attenuation for the vertical component (Fig. 7b) in the study area exhibits significant oscillations in the 2–10 Hz frequency band, but the overall characteristics are consistent with the horizontal geometric attenuation characteristics. Afterwards, we obtained b exponents of −0.51 and −0.53 for the horizontal and vertical components, respectively. In the inversion, six models of the geometric spreading functions were also considered to investigate the geometric attenuation model suitable for the Sichuan Basin region: (1) five simple models with $b = -0.5, -0.6, -0.7, -0.8$ and -1.0 and (2) widely used complex three-stage functions, which are plotted in Figs 6(a) and 7(a). The results indicate that $R^{-0.5}$ or $R^{-0.6}$ may be able to reasonably describe the geometric attenuation characteristics in the Sichuan Basin. Unfortunately, the quality factor estimated by eq. (7) is plotted in Fig. 8(a), which shows that when the geometric spreading function is selected as $R^{-0.6}$, the frequency-related quality factor in some frequency bands appears abnormally high (Castro *et al.* 1990; Salazar *et al.* 2007). Finally, simple models with b equal to −0.5 were selected in our scheme, which is well matched with the geometric attenuation exponent b value of 0.57 given by Wang *et al.* (2018) in the Sichuan region. Before estimating the quality model, we performed a sensitivity test for attenuation transition distance using multiple distances and frequencies, and then, the Q models in the study area were estimated as $Q(f) = 129.9872f^{1.1119}$ for the horizontal component and $Q(f) = 132.54f^{1.1236}$ for the vertical component. In addition, by using the parametric GIT, where the geometric attenuation is defined as $R^{-0.5}$, the quality factors for both the horizontal and vertical components are estimated as $Q(f) = 132.3729f^{0.8409}$ and $Q(f) = 138.0317f^{0.901}$, respectively. The quality factor models are plotted in Fig. 8(b), which indicates that the Q models of the two components obtained from the parametric GIT or non-parametric GIT have small differences. The GIT quality factors were lower than the quality factor values obtained from the non-parametric GIT at high frequencies ($f > 1$ Hz) but higher than the quality factor values obtained from the non-parametric GIT at low frequencies ($f < 1$ Hz).

In general, the regional quality factor is smaller in areas with greater seismic activity. For the Sichuan Basin area, GIT Q models estimated from different geometrical spreading functions were obtained. For example, the quality factor models $Q(f) = 147.5f^{1.13}$ (Fu *et al.* 2019), $Q(f) = 335f^{0.72}$ (Guo *et al.* 2023) and $Q(f) = 217.8f^{0.816}$ (Zhang *et al.*, 2017) have the same complex three-stage geometric spreading function, which is defined as $(1/R)^{-1}$ when R is less than 70.5 km, 1/70.5 when R is between 70.5 and 117.5 km, and $\sqrt{117.5/R}/70$ when R is greater than 117.5 km. In addition, the Q model $Q(f) = 151.2f^{1.06}$ (Wang *et al.* 2018) inverted by Wenchuan aftershocks was also compared in this inversion (Table 2). All the Q models for the horizontal component are plotted in Fig. 8(c), which indicates that the quality factors calculated using the non-parametric GIT in this study are well matched with the inversion results of other studies at high frequencies, while they are well matched with the results of Fu *et al.* (2019) and Wang *et al.* (2018) at low frequencies. However, the quality factor obtained by GIT is significantly smaller than that of other models at high frequencies, resulting from the different geometric spreading functions. The Q model trades-off with the estimated geometrical spreading; therefore, both parameters must be used together. In this inversion, we also compared the total path attenuation obtained from different models with hypocentral distances of 20, 40 and 60 km (Figs 8d–f), which indicated that there is a strong dependence between the total path attenuation and the geometric attenuation model. When the geometric attenuation is the same, the total path attenuation is not significantly different, especially in the high-frequency range ($f > 1$ Hz).

4.2 Site amplification

In this study, to constrain the site effect, strong-motion station 51BCQ, which is located under rock site conditions, was selected, and then the horizontal-to-vertical (H/V) spectral ratio (Lermo & Chavez-Garcia 1993; Ameri *et al.* 2011; Toni, 2017) was calculated, which is plotted in Fig. 9. Similar to the GIT, the trade-off between the source and site components can be addressed by selecting a reference bedrock station at which the site effect can be fixed to unity

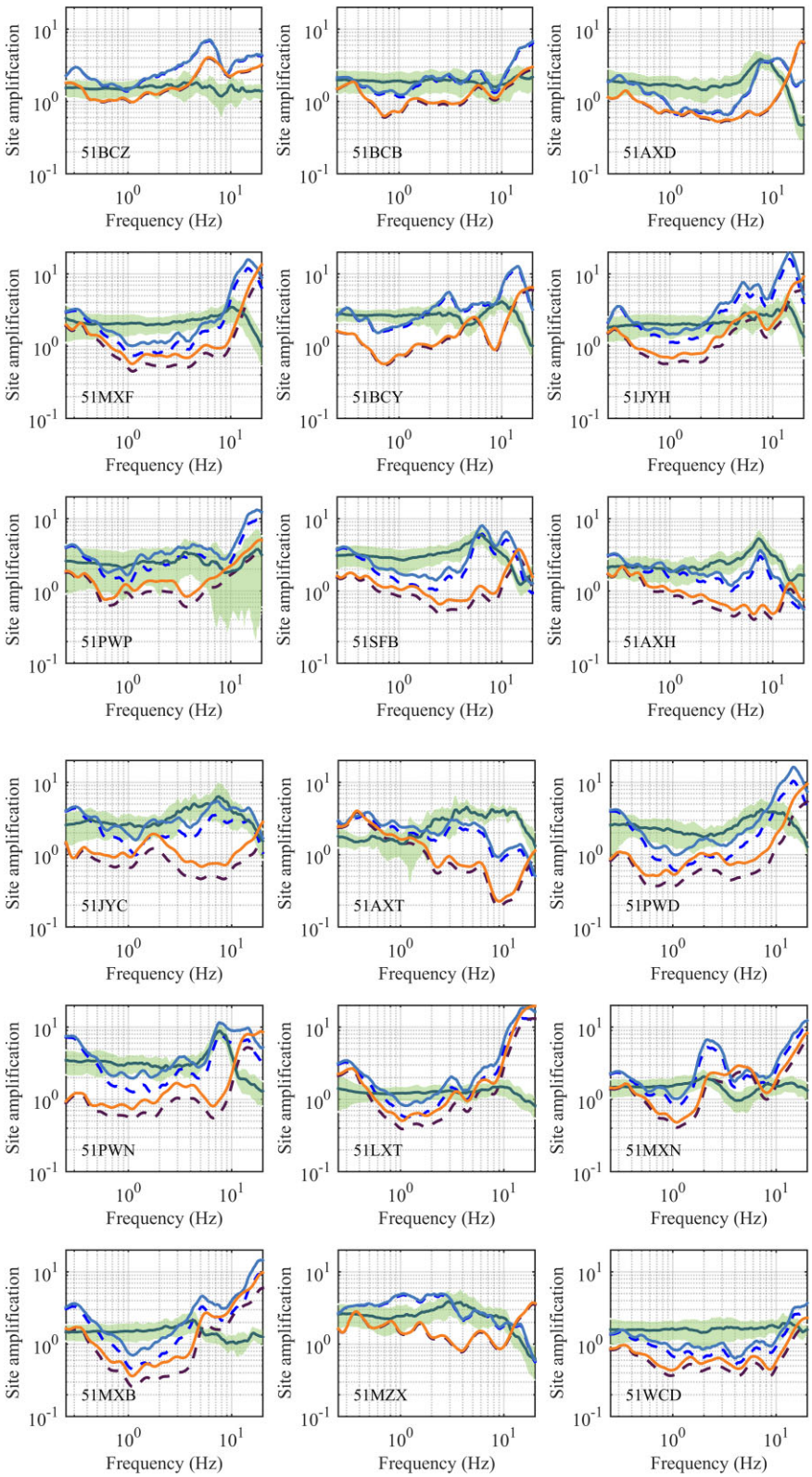

Figure 10. Site amplification estimated via the NONGIT and GIT methods compared with that obtained via the H/V method for 45 strong-motion stations. The NONGIT site amplifications on the horizontal and vertical components are represented by solid lines. All the NONGIT site effects are averaged from the bootstrap analysis. The solid line indicates the average H/V site amplification, and the shaded area indicates the ± standard deviation.

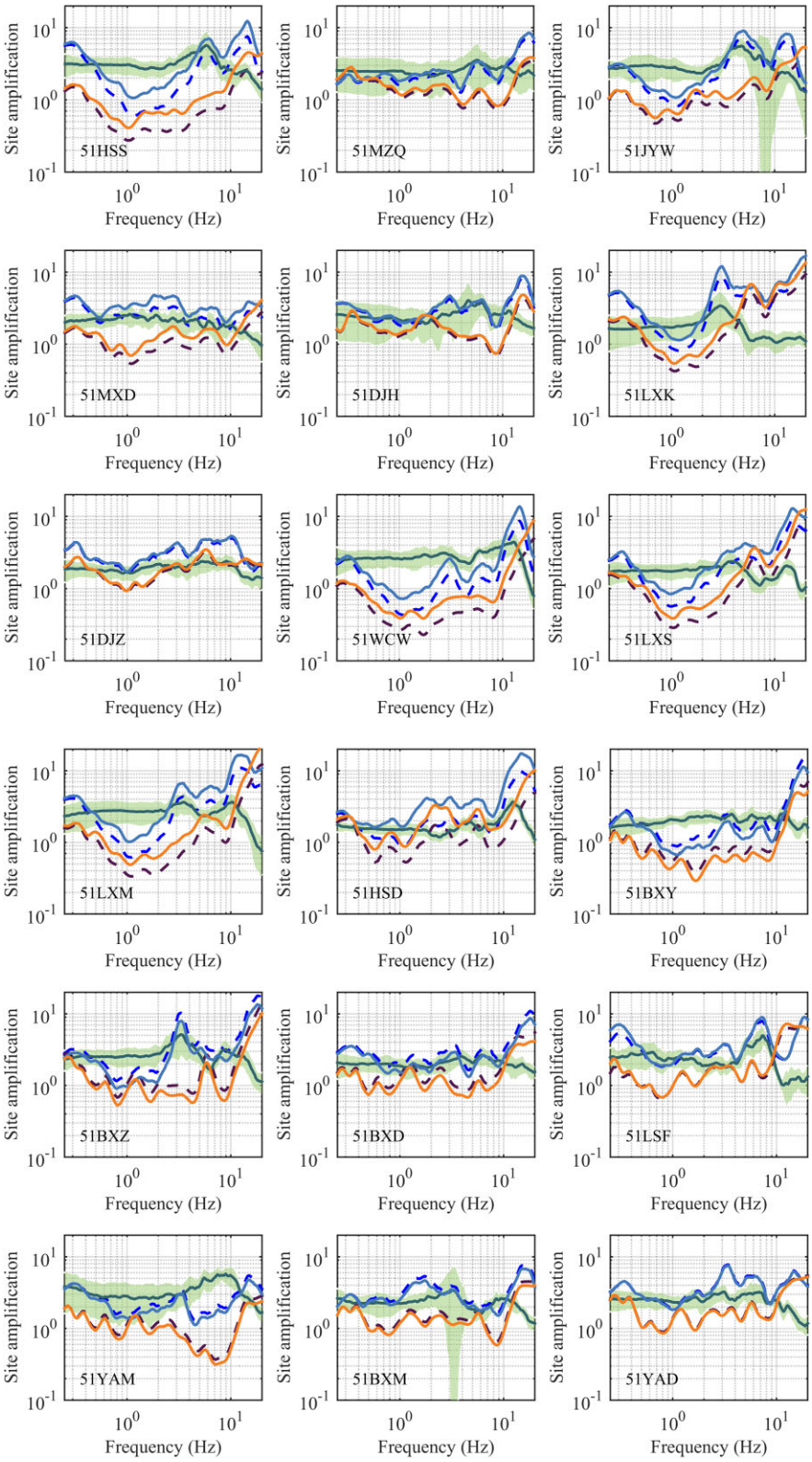

Figure 10. Continued

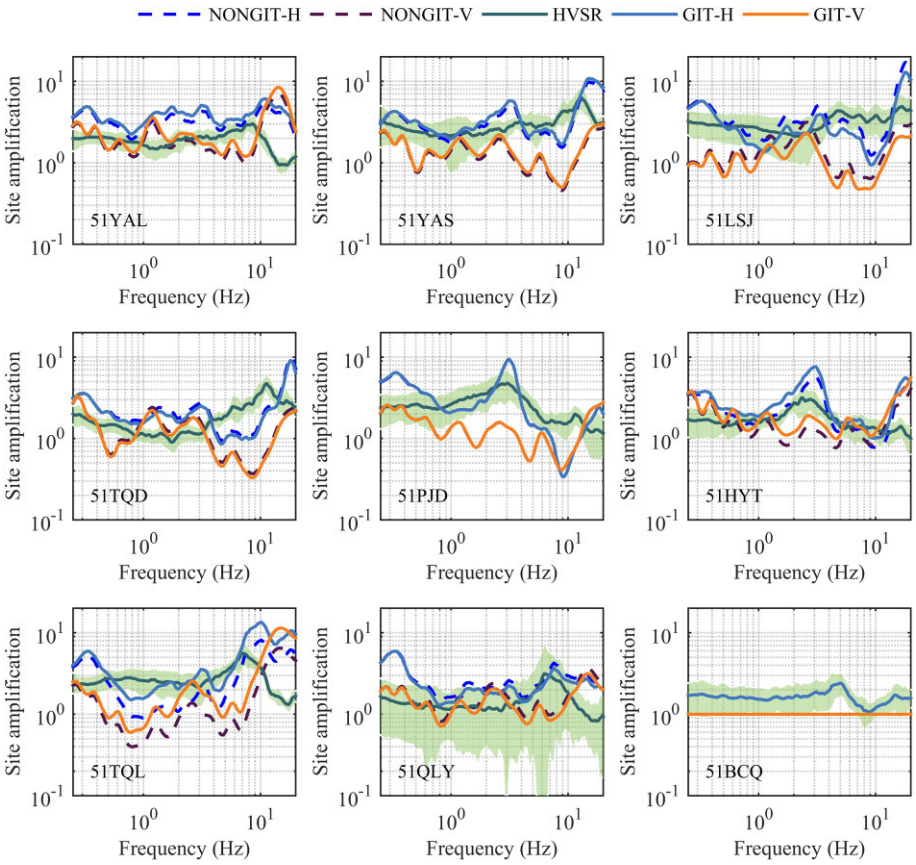

Figure 10. Continued

(Iwata & Irikura 1988; Jeong *et al.* 2020) or selecting an event with known source spectra or source parameters (Boatwright *et al.* 1991; Moya & Irikura 2003). Although the H/V spectrum amplitudes of the 51BCQ station fluctuate significantly between 4 and 10 Hz, the maximum and minimum values are 2.3 and 1.2, respectively, which are not significantly different from the average value of 1.7. This result indicates rough flat shape with low-amplitude amplification. In this case, the site effect at reference station 51BCQ can be considered equal to unity for the vertical component of ground motion (Ameri *et al.* 2011; Mandal & Dutta 2011), and the real H/V ratio was used for the horizontal component. Fig. 10 shows the site effects derived by the non-parametric GIT for both the horizontal and vertical components. Moreover, the average site effects obtained by the H/V ratio and its corresponding ± standard deviation area were also plotted.

The site effects estimated from the non-parametric GIT for the horizontal and vertical components were separately described to investigate the possible amplifications of the vertical component of ground motion, which could lead to issues in explaining the H/V results. The results indicate that there is good consistency between the H/V ratio and the NONGIT horizontal amplification for certain stations, especially indicating that the predominant frequencies are approximately identical. However, at some stations, such as stations 51AXD, 51AXH, 51WCD and 51BXY, the NONGIT site effects are significantly smaller than the site effects obtained by the H/V spectral ratio. Overall, the average of the NONGIT site amplification functions is generally greater than that of the H/V approach. Some previous results have also indicated that the H/V approach usually underestimates site amplification (Bard 1998; Castro *et al.* 2001, 2004; Salazar *et al.* 2007; Hassani *et al.* 2011; Dang *et al.* 2024). In addition, previous studies have proven that the H/V spectral ratio can be used to obtain the predominant frequency while usually underestimating site effects (Castro *et al.* 2004; Ren *et al.* 2013). The reason for this result is related to site amplification of the reference station, which may vary depending on the geological conditions.

Interestingly, the results at several strong-motion stations indicate a significant impact of site amplification on the vertical component of ground motion. Therefore, the main differences between the site effects obtained from H/V and NONGIT occur at stations with remarkable amplification of the vertical component. In this case, the assumption of using the H/V spectra ratio to estimate the site effect is incorrect. These findings are consistent with some studies that use the GIT to calculate site amplification (Castro *et al.* 1997; Bindi *et al.* 2009; Oth *et al.* 2009, 2011; Ameri *et al.* 2011). At stations 51PWN and 51AXD, the H/V and NONGIT curves exhibit the same amplification peak at approximately 8 Hz (51PWN) and 10 Hz (51AXD), while in other frequency bands, the differences between H/V and NONGIT-H are significant due to vertical amplification. At station 51LXK, the predominant frequency obtained by the H/V and NONGIT methods is approximately 3 Hz; when the frequency is higher than 4 Hz, the H/V curve tends to plateau, while the NONGIT-H curve increases with increasing frequency. The vertical amplification of the site results in a marked difference between the H/V and NONGIT-H curves. Interestingly, at station 51LXT, remarkable amplifications appear at frequencies > 9 Hz for both the NONGIT-H and NONGIT-V site effects, which are substantially larger than those estimated by the H/V technique.

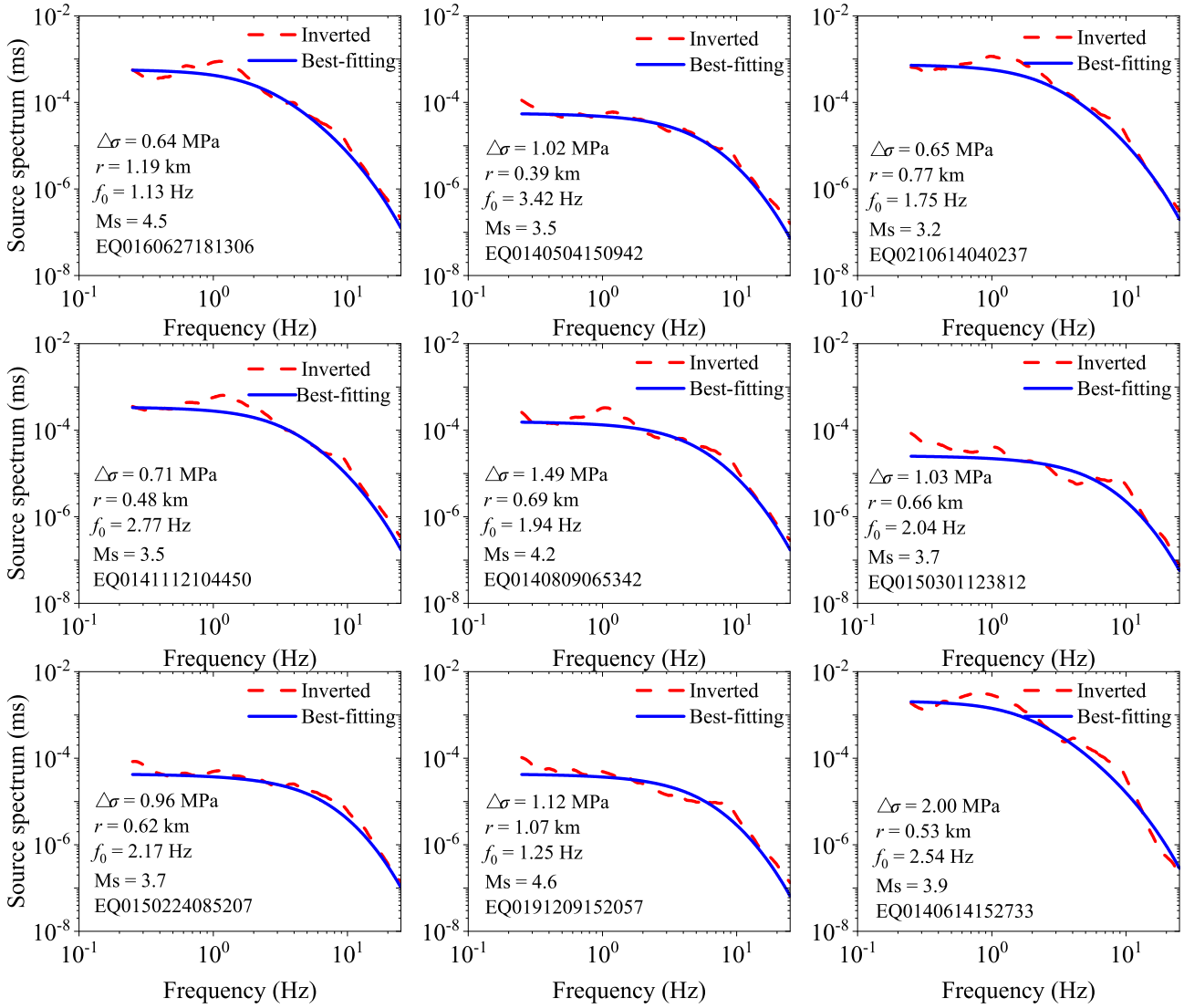

Figure 11. The best-fitted (solid line) and inverted (dashed line) source spectra for selected earthquake events. The dashed line denotes the inverted model from the bootstrap analysis. The source parameters, such as corner frequency f_0, surface wave magnitude M_s, source radius r, stress parameter $\triangle\sigma$ and earthquake name, are also shown in each panel.

There may be some reasons for the amplification of the vertical component. On the one hand, S-P conversion occurs at the bottom of the soft layer under high-impedance constraints (Parolai & Richwalski 2004; Ameri *et al.* 2011; Jeong *et al.* 2020); on the other hand, the presence of *P*-wave trains in the selected *S*-wave windows due to the short distance and the separation between *P* and *S* waves was not feasible (Ameri *et al.* 2011).

4.3 Source spectra

In this study, a bootstrap analysis method given by Oth *et al.* (2011) was adopted to study the stability of the inversion results. The source component that follows Brune's ω^2 model of the ith earthquake event obtained from the GIT can be written as follows (Boore 2003):

$$S(f) = \frac{CM_0(2\pi f)^2}{1+\left(f/f_0\right)^2} \cdot \exp\left(-\pi\kappa_0 f\right), \tag{8}$$

where κ_0 indicates the high-frequency attenuation parameter and the constant C can be defined as follows:

$$C = \frac{\Re_{\theta\varphi} F V}{4\pi\rho\beta^3 R_0}, \tag{9}$$

where $\Re_{\theta\varphi}$, V, F, β and ρ account for the average radiation pattern for the *S* wave, usually set to 0.55, the proportion of *S*-wave energy onto two horizontal components, usually set to 0.707, the free surface amplification usually set to 2, and the *S*-wave velocity and density near the source, respectively. R_0 accounts for the reference distance in km. In this inversion, the reference distance R_0 was set to 13 km, which is the minimum hypocentral distance. M_0 accounts for the seismic moment and f_0 represents the corner frequency.

The high-frequency attenuation parameter was obtained by using robust linear regression in the form of $\kappa = \kappa_0 + m \times R$ (Andrew & Hough 1984; Dang *et al.* 2022), in which m (s km^{-1}) and R (km) indicate the coefficient and fault distance, respectively. Then, the relation between the high-frequency attenuation parameter and distance was estimated to be $\kappa = 0.0471 + 0.0000918R$ for the Sichuan

Table 3. Source parameters, such as corner frequency f_0, moment magnitude M_w, seismic moment M_0, radius r and stress drop $\triangle\sigma$, calculated by the GIT method.

Event ID	Event name	Lat	Lon	M_s (M_L)	f_0	M_w	M_0	r	$\triangle\sigma$
1	**EQ190225084000**	29.46	104.50	4.3 (4.8)	1.47	4.02	12.2	910	0.71
2	EQ160627181306	31.89	104.41	4.5 (4.9)	1.13	4.23	24.4	1190	0.64
3	**EQ140817060800**	28.12	103.51	5.2 (5.6)	1.31	4.45	53.9	1020	2.22
4	**EQ190225131559**	29.48	104.49	4.9 (5.3)	1.08	4.31	32.8	1250	0.74
5	EQ150301123812	31.78	104.08	3.7 (4.2)	2.04	3.85	6.68	660	1.03
6	EQ161205142525	31.89	104.46	**3.1** (3.7)	2.36	3.55	2.37	570	0.57
7	EQ191209152057	31.56	104.25	4.6 (5.0)	1.25	4.30	31.6	1070	1.12
8	EQ150831215606	31.90	104.40	3.6 (4.1)	2.61	3.70	3.98	510	1.29
9	EQ130316204500	31.90	104.30	3.9 (4.4)	2.20	3.70	3.98	610	0.77
10	EQ110323080308	31.71	104.01	3.9 (4.4)	2.08	4.00	11.2	640	1.84
11	EQ140402140443	31.17	103.60	4.2 (4.7)	1.98	3.93	8.66	680	1.22
12	EQ130127130647	31.52	103.26	4.2 (4.7)	1.63	3.93	8.66	820	0.68
13	EQ190502155758	30.43	103.01	4.5 (4.9)	1.23	4.30	31.6	1090	1.06
14	**EQ190516043331**	28.07	103.53	4.7 (5.1)	1.21	4.22	23.6	1110	0.75
15	EQ110605132145	31.80	104.14	4.2 (4.7)	1.36	4.15	18.8	990	0.86
16	EQ130420083138	30.39	103.01	4.5 (4.9)	1.59	4.08	14.5	840	1.06
17	EQ160529101438	31.46	104.30	4.4 (4.8)	2.06	4.00	11.2	650	1.79
18	EQ160521015503	31.52	103.28	**3.5** (4.1)	2.16	3.78	5.16	620	0.95
19	EQ120702061759	31.72	103.51	4.0 (4.5)	2.49	3.93	8.66	540	2.42
20	EQ140504150942	31.93	104.48	3.5 (4.1)	3.42	3.40	1.41	390	1.02
21	EQ150224085207	31.66	104.02	3.7 (4.2)	2.17	3.78	5.16	620	0.96
22	EQ130420185902	30.40	103.00	4.1 (4.6)	1.49	4.08	14.5	900	0.87
23	**EQ180706131945**	30.36	103.28	3.6 (4.1)	2.13	3.69	3.83	630	0.67
24	**EQ190703122653**	28.40	104.85	4.8 (5.2)	1.08	4.26	27.8	1240	0.65
25	**EQ190622222956**	28.43	104.77	5.4 (5.7)	0.85	4.55	75.1	1580	0.84
26	EQ161202103543	31.99	104.48	**3.1** (3.7)	2.94	3.55	2.37	460	1.10
27	EQ210614040237	31.99	104.49	**3.2** (3.8)	1.75	3.85	6.68	770	0.65
28	EQ120527191901	31.47	103.95	4.0 (4.5)	2.26	3.78	5.16	590	1.08
29	EQ110401130712	31.59	104.01	4.0 (4.5)	2.59	3.93	8.66	520	2.73
30	EQ151211052745	32.00	104.52	3.7 (4.2)	3.56	3.63	3.07	380	2.53
31	EQ130420103837	30.25	103.01	4.7 (5.1)	1.09	4.30	31.6	1230	0.74
32	EQ141216110340	30.31	103.06	3.6 (4.1)	3.12	3.55	2.37	430	1.30
33	EQ141112104450	31.81	104.14	3.5 (4.1)	2.77	3.48	1.83	480	0.71
34	EQ150812071153	31.24	103.64	3.8 (4.3)	2.79	3.78	5.16	480	2.03
35	EQ171106083412	31.22	103.70	**3.2** (3.8)	1.92	3.93	8.66	700	1.12
36	EQ130421170524	30.34	103.00	5.4 (5.7)	0.77	4.68	115.0	1730	0.97
37	EQ130420191250	30.35	103.02	4.3 (4.8)	1.92	4.15	18.8	700	2.42
38	EQ130421115939	30.26	103.00	4.9 (5.3)	1.01	4.45	53.1	1330	1.00
39	EQ140809065342	31.83	104.13	4.2 (4.7)	1.94	4.00	11.2	690	1.49
40	EQ110116083016	31.98	104.48	4.1 (4.6)	2.54	3.93	8.66	530	2.57
41	EQ140611224647	31.25	103.59	3.5 (4.1)	3.71	3.40	1.41	360	1.31
42	EQ140411103058	31.70	103.18	4.9 (5.3)	1.33	4.38	41.0	1010	1.74
43	EQ130423055450	30.35	103.00	4.3 (4.8)	1.83	4.15	18.8	730	2.08
44	EQ141215003515	30.36	103.05	3.7 (4.2)	3.37	3.63	3.07	400	2.14
45	EQ110507082112	31.52	103.83	3.9 (4.4)	1.98	4.08	14.5	680	2.06
46	EQ130309202358	31.35	103.50	4.2 (4.7)	2.13	4.00	11.2	630	1.97
47	EQ140310191723	31.64	104.03	3.7 (4.2)	4.14	3.55	2.37	320	3.05
48	EQ140522104733	31.63	103.92	**2.9** (3.5)	3.11	3.48	1.83	430	1.00
49	EQ121008230558	31.42	103.92	**3.7** (4.2)	2.67	3.78	5.16	500	1.79
50	EQ130105130613	31.66	104.11	**3.9** (4.4)	2.12	3.85	6.68	630	1.15
51	EQ130421184824	30.30	103.00	4.2 (4.7)	1.51	4.08	14.5	890	0.91
52	EQ130420174514	30.31	103.04	4.0 (4.5)	1.81	4.00	11.2	740	1.20
53	EQ130420151834	30.39	103.00	4.2 (4.7)	1.94	3.93	8.66	690	1.15
54	EQ160330091412	31.41	103.81	**3.0** (3.6)	3.49	3.48	1.83	380	1.41
55	EQ121201231644	31.85	104.18	4.3 (4.8)	1.83	4.15	18.8	730	2.08
56	EQ120611235358	31.32	103.46	**3.9** (4.4)	1.99	3.93	8.66	680	1.23
57	EQ170423052657	31.42	103.97	**3.3** (3.9)	1.67	3.93	8.66	800	0.73
58	EQ200122150833	31.66	103.13	4.5 (4.9)	1.18	4.23	24.4	1140	0.73
59	EQ120302084621	31.33	103.68	**3.2** (3.8)	3.55	3.55	2.37	380	1.93
60	EQ130708073914	31.28	103.57	**4.0** (4.5)	2.31	3.93	8.66	580	1.95
61	**EQ140405064033**	28.14	103.57	5.1 (5.5)	1.09	4.41	45.7	1240	1.06
62	EQ170606140457	31.32	103.20	**3.3** (3.9)	1.84	3.93	8.66	730	0.98
63	EQ110904121345	31.27	103.62	4.2 (4.7)	1.57	4.15	18.8	850	1.33
64	EQ140614152733	31.56	104.13	3.9 (4.4)	2.54	3.85	6.68	530	2.00

Table 3. Continued

Event ID	Event name	Lat	Lon	M_s (M_L)	f_0	M_w	M_0	r	$\Delta\sigma$
65	**EQ190704101758**	28.41	104.74	5.6 (5.9)	0.72	4.65	105.0	1860	0.71
66	EQ111226004652	31.37	103.79	4.7 (5.1)	1.40	4.38	41.0	960	2.04
67	EQ130421045344	30.36	103.05	5.4 (5.7)	1.26	4.45	53.1	1070	1.91
68	EQ201021120447	31.84	104.17	4.6 (5.0)	1.49	4.30	31.6	900	1.92
69	EQ171110110315	31.57	103.93	4.3 (4.8)	1.96	4.08	14.5	680	1.99
70	**EQ190617233601**	28.43	104.77	5.1 (5.5)	0.71	4.75	150.0	1880	0.98
71	EQ201022110347	31.83	104.18	4.7 (5.1)	1.03	4.45	53.1	1300	1.05
72	EQ140711195643	29.63	103.09	3.7 (4.2)	3.73	3.63	3.07	360	2.90
73	EQ110506184815	31.26	103.59	4.1 (4.6)	1.61	3.93	8.66	830	0.65
74	EQ120405063249	31.99	103.05	**3.6** (4.1)	1.92	3.85	6.68	700	0.86
75	EQ130808025143	31.69	103.18	**4.2** (4.7)	1.36	4.15	18.8	990	0.86
76	EQ141106145421	31.26	103.23	3.8 (4.3)	3.70	3.63	3.07	360	2.83
77	**EQ190617225543**	28.34	104.90	6.0 (6.3)	0.47	5.05	422.0	2850	0.80
78	**EQ210916043300**	29.20	105.34	6.0 (6.3)	0.59	4.84	202.0	2290	0.74

Unit: Latitude, °; Longitude, °; f_0, Hz; M_0, ($\times 10^{14}$ Nm); r, m; $\Delta\sigma$, MPa;
The event ID can be divided into data and time of this earthquake. For example, EQ190225084000 indicates that the earthquake occurred on 2019 February 25 at 08:40:00 (Beijing time). The bold character indicates that Ms is calculated from the empirical relationship Ms = 1.13M_L−1.08 (Wang *et al.* 2010). The bold characters indicate the data set used for parametric GIT.

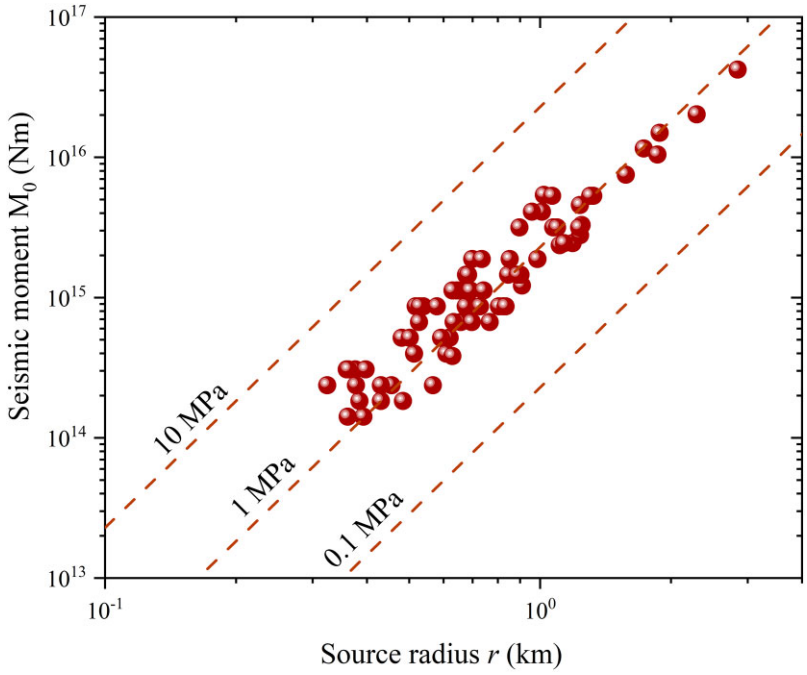

Figure 12. The moment magnitude M_0 versus source radius r. The balls represent the earthquake events used in our scheme. The dashed lines from bottom to top indicate the constant stress drop relationships corresponding to 0.1, 1 and 10 MPa.

Basin region (Fu *et al.* 2019). Therefore, a κ_0 value of 0.0471 was adopted. In this study, an iterative least-squares inversion method based on the Levenberg−Marquardt algorithm (Fletcher 1995) was used to calculate the seismic moment M_0 and corner frequency f_0 for each selected earthquake event. Then, the empirical relationship between the moment magnitude M_w and the seismic moment M_0 (Nm) given by Hanks & Kanamori (1979) was applied to calculate the moment magnitude.

The inverted source spectra obtained from the non-parametric GIT are plotted in Fig. 11. In each panel, the best-fitting model with an ω^2 shape was compared with the inverted values. The results indicate that the inverted source spectra are very consistent with Brune's spectra for each event. The widely used earthquake source model is defined as the ω^2 model (Brune 1970). In this case, the source radius and the stress parameter for each selected earthquake event can be obtained as follows:

$$r_i = \frac{2.34\beta}{2\pi f_{0i}} \tag{10}$$

$$\Delta\sigma_i = \frac{7M_{0i}}{16r_i^3} \times 10^6, \tag{11}$$

where r_i denotes the source radius (m) and $\Delta\sigma_i$ indicates the stress parameter (MPa). The remaining parameters, such as β and M_{0i}, are in m s^{-1} and Nm, respectively. The source parameters mentioned above for representative earthquake events are also listed in each panel of Fig. 11. A detailed summary of the source parameters for all 78 selected events is shown in Table 3. The results indicate that the inverted source parameters generally conform to source scaling,

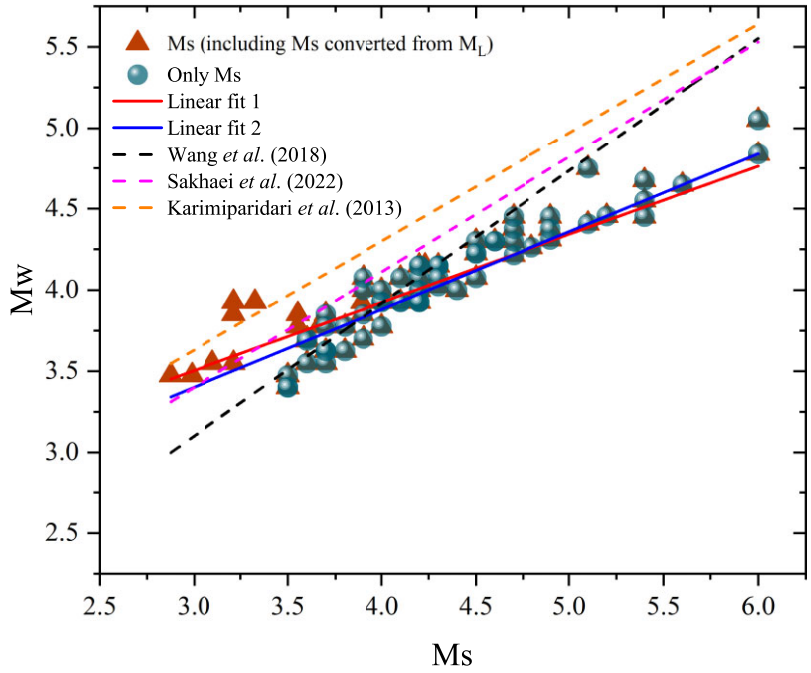

Figure 13. Comparison between the moment magnitude (M_w) estimated by the source spectra and the surface wave magnitude M_s. The triangles and balls indicate the M_s (including the M_s converted from the M_L) and the M_s (only), respectively. The solid lines indicate the best-fitting models. The dashed lines indicate the relationships between M_s and M_w given by Wang *et al.* (2018), Sakhaei *et al.* (2022) and Karimiparidari *et al.* (2013), respectively.

and the moment magnitudes inverted in this inversion are smaller than the surface wave magnitude M_s or the local magnitude M_L, which is consistent with the results from other regions in China (Matsunami *et al.* 2003; Xu *et al.*, 2010; Zhao *et al.* 2011; Lyu *et al.* 2013; Wang *et al.* 2018).

Fig. 12 displays the relationship between the seismic moment M_0 and source radius r and compares it with constant stress parameter laws of 0.1, 1.0 and 10 MPa, indicating that the stress calculated in this study ranges between 0.3 and 2.6 MPa with a mean value of 1.1 MPa, which is smaller than the average stress parameter of 4.89 MPa for global intraplate earthquakes (Allmann & Shearer, 2009) and slightly lower than the stress parameter of 1.5 MPa for the 2013 Lushan M_w 6.6 earthquake (Hao *et al.* 2013). The result obtained in this inversion is well matched with the results inverted by Zhou *et al.* (2022) for the Yangbi region.

Fig. 13 compares the seismic moment M_w derived from source spectra with the surface wave magnitude M_s and local magnitude M_L. In this study, both the M_s and M_L data were obtained from the China Earthquake Network Centre. On the one hand, the relation between M_w and M_s was estimated to be $M_w = 0.4784M_s + 2.0234$, without considering the M_s converted through M_L. On the other hand, we obtained the M_s for the corresponding event converted through the M_L with the relation $M_s = 1.13M_L - 1.08$ (Wang *et al.* 2010), and then, the relationship between M_w and M_s was estimated as $M_w = 0.5557M_s + 1.6603$. Fig. 13 shows that both models obtained in this study agree well with other relationships, especially with the models of Wang *et al.* (2018) and Sakhaei *et al.* (2022).

4.4 Inversion residual

Fig. 14 shows that the site amplifications calculated by the NONGIT and H/V methods were averaged at several frequency points ranging from 1 to 16 Hz with an interval of 1 Hz. The comparison between the inversion results obtained by the NONGIT and H/V methods indicates that at frequencies of $f < 5$ Hz, the site amplification obtained by the NONGIT method is smaller than that estimated by the H/V method, while at frequencies of $f > 13$ Hz, the opposite is true, which indicates that a strong amplification effect occurs at low frequencies in the basin. These results are consistent with the conclusions of Fu *et al.* (2019). In other frequency bands, the site effects obtained by both methods are in good agreement. The reason for this result may be whether the average velocity of shear waves in the top 30 m of soil is adequate for soil or rock classification (Hassani *et al.* 2011).

In addition, a residual defined as a function of the hypocentral distance (R_{hyp}) and surface wave magnitude (M_s) was adopted to analyse the bias in the inversion results. The residuals are defined as the natural logarithm (ln) of the ratio of the recorded and synthetized FAS values (i.e. ln(Obs/Sim)). The relationships among the residuals and the hypocentral distance and magnitude are plotted in Figs 15 and 16, which indicate that there is no significant bias in the residuals. In addition, the residuals show no obvious dependence of the scatter on distance or magnitude. It is worth confirming that the inversion results are reliable and stable. Therefore, the spectral parameters obtained in this study can be used to reconstruct the median ground motion in the Sichuan Basin, China.

5. CONCLUSIONS

In this study, we presented the results estimated using the non-parametric GIT for seismic recordings recorded by 45 strong-motion stations. The GIT has always been used to separate the source, path and site components of earthquake ground motions; thus, source parameters, such as the stress drop, corner frequency, moment magnitude and source radius, and path parameters, such as the frequency-dependent $Q(f)$ model and geometric propagation model, can aid in the study of seismic disasters and risk assessment in the study region (Ameri *et al.* 2011).

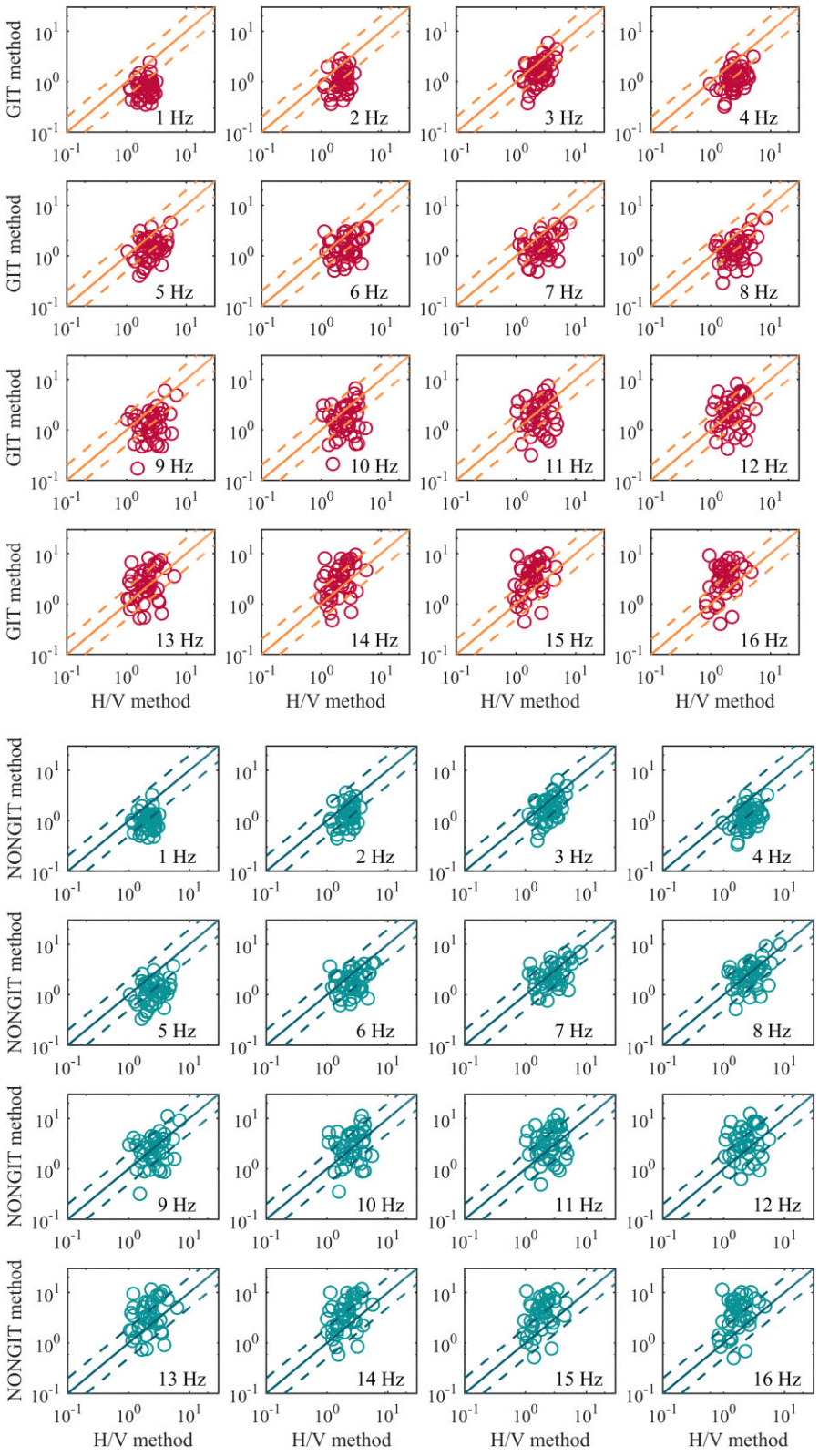

Figure 14. Comparison of site amplification between the NONGIT, GIT and H/V methods at 16 selected frequency points. The circles represent the site amplification averaged over all strong motion stations. The dashed and solid lines indicate the 1:2, 2:1 and 1:1 correspondence.

1. The path attenuation decays significantly with distance when the distance is smaller than 45 km, while at larger distances, the attenuation is slow and gradually tends to plateau. In addition, the path attenuation of *S* waves for both horizontal and vertical components with higher frequencies showed a decreasing attenuation compared to lower frequencies. We compared five simple models and a complex geometric attenuation model. Finally, a simple model with b equal to -0.5 was selected to describe the geometric spreading.

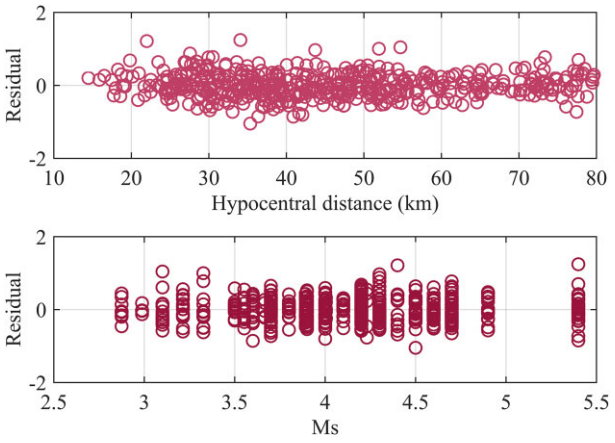

Figure 15. Residual of the FAS versus the hypocentral distance (top) and surface wave magnitude M_s (bottom).

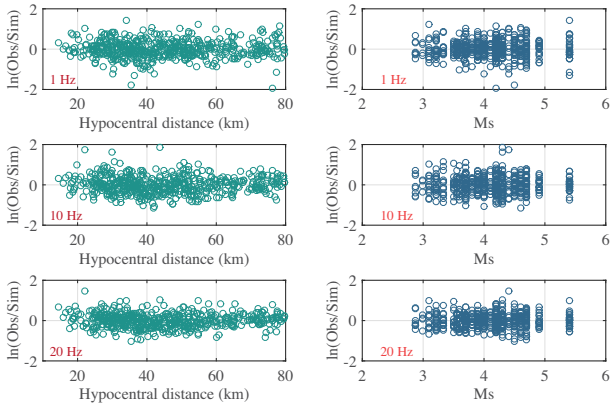

Figure 16. Residual (=ln(Obs/Sim)) of FAS at frequency points of 1.0, 10.0 and 20.0 Hz. The residual was defined as a function of the hypocentral distance (left panel) and surface wave magnitude (right panel).

Then, the regional quality factor Q in the study area was estimated to be $Q(f) = 129.9872f^{1.1119}$ for the horizontal component and $Q(f) = 132.54f^{1.1236}$ for the vertical component. For comparison, we used the parametric GIT to estimate the quality factor, which can be written as $Q(f) = 132.3729f^{0.8409}$ for the horizontal component and $Q(f) = 138.0317f^{0.901}$ for the vertical component. The results indicate that the Q models of the two components obtained from the parametric GIT or non-parametric GIT have small differences.

2. The site effects obtained from the non-parametric GIT and H/V methods indicate that there is good consistency between the H/V method and the NONGIT horizontal amplification for certain stations, especially indicating that the predominant frequencies are approximately identical. However, we observed that the vertical component of the ground motion exhibits significant amplification characteristics at several strong-motion stations. At these stations, the H/V spectral ratio method cannot be adopted to estimate the amplitude curves and, in some cases, the predominant frequency. In this study, most stations are located on the edge of the Sichuan Basin, which may have amplified the vertical component.

3. A comparison between the inverted and best-fitting source spectra indicates that the inverted source parameters generally conform to source scaling. The stress parameters obtained for the earthquake events selected in this inversion vary between 0.3 and 3.5 MPa, with a mean value of 1.36 MPa. The stress drop inverted in this study is lower than the average stress parameter of 4.89 MPa for global intraplate earthquakes (Allmann & Shearer, 2009) and is slightly lower than the stress parameter of 1.5 MPa for the 2013 Lushan M_w 6.6 earthquake (Hao *et al.* 2013). However, this result is well matched with the results inverted by Zhou *et al.* (2022) for the Yangbi region. In addition, the relation between the moment magnitude and surface wave magnitude was obtained as $M_w = 0.4784M_s + 2.0234$, without considering the M_s converted through M_L. After the M_L was converted to M_s, the relationship was estimated as $M_w = 0.5557M_s + 1.6603$. These two models are well matched with the model given by Wang *et al.* (2018).

DATA AVAILABILITY

The acceleration waveforms were provided by the China Strong Motion Network Centre at https://data.earthquake.cn/datashare/report.shtml?PAGEID=datasourcelist&dt=40280d0453e5add30153e5e79dc6001b (last accessed December 2022) upon reasonable request (email: csmnc@iem.ac.cn). Earthquake parameters, including hypocentre location, measured magnitude M_s and local magnitudes M_L were obtained from China Earthquake Network Center at https://data.earthquake.cn/datashare/report.shtml?PAGEID=datasourcelist&dt=40280d0453e5add30153e5e79dc6001b, (last accessed May 2023). The NONGIT method can be found at https://doi.org/10.1785/0120200097 (Jeong *et al.* 2020), which was used for estimating source characteristics, site effects and path attenuation. Moment magnitude M_w in the Global Centroid–Moment–Tensor catalogue was obtained from http://www.globalcmt.org/CMTsearch.html, (last accessed May 2023). Some plots, such as Fig. 1, was made using the Generic Mapping Tools (GMT) version 5.2.1 (Wessel *et al.*, 2013), which can be downloaded from the website at https://www.generic-mapping-tools.org/ (last accessed May 2018), and some figures, such as Figs 10, 14, 15 and 16 were prepared using the MATLAB software, which can be downloaded from the website at https://www.mathworks.cn/campaigns/products/trials.html (last accessed May 2018). The remaining figures were made using the Origin software (https://www.originlab.com/, last accessed May 2018). The relationship between surface wave magnitude M_s and local magnitude M_L can be available at https://blog.sciencenet.cn/blog-575926-686661.html (last accessed August 2023). The FAS values of the reference station 51BCQ can be found in the Supplementary section.

ACKNOWLEDGMENTS

The authors are thankful to the CSMNC for providing the strong-motion data used in this study. The authors sincerely thank American Journal Experts (https://www.aje.com) for providing the linguistic assistance during the preparation of the original manuscript. Finally, the authors would like to express gratitude to the Assistant Editor Louise Alexander, Editor Eiichi Fukuyama, and two anonymous reviewers for their valuable comments that improved the study. This study was supported by the National Natural Science Foundation of China (No. 42204050), the Exploration Fund of Zhejiang Natural Science Foundation (Grant No. ZX2024000700), the Hong Kong Research Grant Council Grants (Nos. 14303721, 14306122 and 14308523), Faculty of Science in The Chinese University of Hong Kong, and the National Natural Science Foundation of China (No. U2139203).

AUTHOR CONTRIBUTIONS

PD contributed to the study conception and design. Material preparation and data collection were performed by PD and JS. All figures were made by PD and the analysis was performed by PD, JS and JC. The original and modified versions of the manuscript were written by PD. All authors commented on previous versions of the manuscript and approved the final manuscript.

SUPPORTING INFORMATION

Supplementary data are available at *GJIRAS* online.

Figure S1. The response spectra of 13 earthquake records from reference station 51BCQ.

Please note: Oxford University Press is not responsible for the content or functionality of any supporting materials supplied by the authors. Any queries (other than missing material) should be directed to the corresponding author for the paper.

CONFLICT OF INTEREST

The authors acknowledge that there are no conflicts of interest recorded.

REFERENCES

Ahmadzadeh, S., Parolai, S., Javan Doloei, G. & Oth, A., 2017. Attenuation characteristics, source parameters and site effects from inversion of S waves of the March 31, 2006 Silakhor aftershocks, *Ann. Geophys.,* **60,** 668.

Allmann, B.P. & Shearer, P.M., 2009. Global variations of stress drop for moderate to large earthquakes, *J. geophys. Res.,* **114**(1B), B01310. doi: 10.1029/2008JB005821

Ameri, G., Oth, A., Pilz, M., Bindi, D., Parolai, S., Luzi, L., Mucciarelli, M. & Cultrera, G., 2011. Separation of source and site effects by generalized inversion technique using the aftershock recordings of the 2009 L'Aquila earthquake, *Bull. Earthq. Eng.,* **9,** 717–739.

Anderson, J. & Hough, S., 1984. A model for the shape of the Fourier amplitude spectrum of acceleration at high frequencies, *Bull. seism. Soc. Am.,* **74,** 1969–1993.

Andrews, D.J., 1986. *Objective Determination of Source Parameters and Similarity of Earthquakes of Different Size,* in *Earthquake Source Mechanics,* eds Das, S., Boatwright, J. & Scholz, C. H., pp. 259–267, American Geophysical Union.

Askan, A., Sisman, F.N. & Pekcan, O., 2014. A regional near-surface high frequency spectral attenuation (kappa) model for northwestern Turkey, *Soil Dyn. Earthq. Eng.,* **65,** 113–125.

Bard, P.Y., 1998. Microtremor measurements: a tool for site effect estimation?, in *Proceedings of the 2nd International Symposium on Effects of Surface Geology on Seismic Motion,* Yokohama, Japan, **3,** 1251–1282.

Bindi, D., Pacor, F., Luzi, L., Massa, M. & Ameri, G., 2009. The M_w6.3, 2009 L'Aquila earthquake: source, path and site effects from spectral analysis of strong motion data, *Geophys. J. Int.,* **179,** 1573–1579.

Boatwright, J., Fletcher, J.B. & Fumal, T.E., 1991. A general inversion scheme for source, site, and propagation characteristics using multiply records sets of moderate-sized earthquakes, *Bull. seism. Soc. Am.,* **81**(5), 1754–1782.

Boore, D.M., 2003. Stochastic simulation of high-frequency ground motion based on seismological models of the radiated spectra, *Bull. seism. Soc. Am.,* **73**(6A), 1865–1894.

Boore, D.M., 2003. Simulation of ground motion using the stochastic method, *Pure appl. Geophys.,* **160**(3-4), 635–676.

Brune, J., 1970. Tectonic stress and spectra of seismic shear waves from earthquakes, *J. geophys. Res.,* **75,** 4997–5009.

Campbell, K.W., 2009. Estimates of shear-wave Q and κ_0 for unconsolidated and semiconsolidated sediments in Eastern North America, *Bull. seism. Soc. Am.,* **99**(4), 2365–2392.

Castro, R.R., Anderson, J.G. & Singh, S.K., 1990. Site response, attenuation and source spectra of *S*-waves along the Guerrero, Mexico, subduction zone, *Bull. seism. Soc. Am.,* **80,** 1481–1503. doi: 10.1785/BSSA08006A1481

Castro, R.R., Mucciarelli, M., Pacor, F. & Petrungaro, C., 1997. *S*-wave site-response estimates using horizontal-to-vertical spectral ratios, *Bull. seism. Soc. Am.,* **87,** 256–260.

Castro, R.R., Pacor, F., Bindi, D. & Franceschina, G., 2004. Site response of strong motion stations in the Umbria, central Italy, region, *Bull. seism. Soc. Am.,* **94,** 576–590.

Castro, R.R., Rovelli, A., Cocco, M., Di Bona, M. & Pacor, F., 2001. Stochastic simulation of strong-motion records from the 26 September 1997 (M_w 6), Umbria-Marche (Central Italy) earthquake, *Bull. seism. Soc. Am.,* **91,** 27–39.

Chen, C. & Xu, Y., 2013. Relocation of the Lushan M_s 7.0 earthquake sequence and its tectonic implication, *Chin. J. Geophys.,* **56**(12), 4028–4036. (in Chinese)

Dang, P.F., Cui, J. & Liu, Q.F., 2022. Parameter estimation for predicting near-fault strong ground motion and its application to Lushan earthquake in China, *Soil Dyn. Earthq. Eng.,* **156,** 107223. doi: 10.1016/j.soildyn.2022.107223

Dang, P.F., Cui, J., Liu, Q.F. & Li, Y.D., 2023. *Simulation of earthquake ground motion via stochastic finite-fault modeling considering the effect of rupture velocity*, *Stochastic Environmental Research and Risk Assessment,* **37**(6), 2225–2241.

Dang, P.F., Cui, J., Yang, H.F. & Song, J., 2024. Regional spectral characteristics, quality factor and site responses in western-central Sichuan, China (I): application of parametric generalized inversion technique, *Soil Dyn. Earthq. Eng.,* **176,** 108303. doi: 10.1016/j.soildyn.2023.108303

Fernández, C., Nozu, A., Crempien, J.G.F. & Juan, C.,d.L.L., 2022. *Simulation of pulse-like ground motions during the 2015 M_w 8.3 Illapel earthquake with a new source model using corrected empirical Green's functions*, *Seismol. Res. Lett.,* **93**(1), 76–90.

Fletcher, J.B., 1995. Source parameters and crustal *Q* for four earthquakes in South Carolina, *Seismol. Res. Lett.,* **85,** 1127–1143.

Fu, L., Li, X.J., Wang, F. & Chen, S., 2019. A study of site response and regional attenuation in the Longmen Shan region, eastern Tibetan Plateau, SW China, from seismic recordings using the generalized inversion method, *J. Asian Earth Sci.,* **181,** 103887. doi: 10.1016/j.jseaes.2019.103887

Grendas, I., Theodoulidis, N., Hatzidimitriou, P., Margaris, B. & Drouet, S., 2018. Determination of source, path and site parameters based on nonlinear inversion of accelerometric data in Greece, *Bull. Earthq. Eng.,* **16,** 5061–5094.

Guo, Z., Guan, M.L. & Chapman, M.C., 2023. Amplification and attenuation due to geologic conditions in the Sichuan Basin, Central China, *Seismol. Res. Lett.,* **94**(1), 399–413.

Hanks, T.C., 1982. f_{max}, *Bull. seism. Soc. Am.,* **72,** 1867–1879.

Hanks, T.C. & Kanamori, H., 1979. A moment magnitude scale, *J. geophys. Res.,* **84,** 2348–2350.

Hao, J.L., Ji, C., Wang, W.M. & Yao, Z.X., 2013. Rupture history of the 2013 Mw 6.6 Lushan earthquake constrained with local strong motion and teleseismic body and surface waves, *Geophys. Res. Lett.,* **40**(20), 5371–5376.

Hassani, B., Zafarani, H., Farjoodi, J. & Ansari, A., 2011. Estimation of site amplification, attenuation and source spectra of S-waves in the East-Central Iran, *Soil Dyn. Earthq. Eng.,* **31,** 1397–1413.

Husid, P., 1967. *Gravity Effects on the Earthquake Response of Yielding Structures*. Report of Earthquake Engineering Research, Laboratory Pasadena, California Institute of Technology.

Iwata, T. & Irikura, K., 1988. Source parameters of the 1983 Japan sea earthquake sequence, *J. Phys. Earth,* **36**(4), 155–184.

Jeong, S.J., Stump, B.W. & DeShon, H.R., 2020. Spectral characteristics of ground motion from induced earthquakes in the Fort Worth Basin, Texas,

using the generalized inversion technique, *Bull. seism. Soc. Am.,* **110**(5), 2058–2076.

Kale, O., Akkar, S., Ansari, A. & Hamzehloo, H., 2015. A ground-motion predictive model for Iran and Turkey for horizontal PGA, PGV, and 5% damped response spectrum: investigation of possible regional effects, *Bull. seism. Soc. Am.,* **105**(2A), 963–980.

Karimiparidari, S., Zare, M., Memarian, H. & Kijko, A., 2013. Iranian earthquakes, a uniform catalog with moment magnitudes, *J. Seismol.,* **17**(3), 897–911.

Klin, P., Laurenzano, G. & Priolo, E., 2018. GITANES: a MATLAB package for estimation of site spectral amplification with the generalized inversion technique, *Seismol. Res. Lett.,* **89**(1), 182–190.

Konno, K. & Ohmachi, T., 1998. Ground-motion characteristics estimated from spectral ratio between horizontal and vertical components of microtremor, *Bull. seism. Soc. Am.,* **88,** 228–241.

Lermo, J. & Chavez-Garcia, F.J., 1993. Site effect evaluation using spectral ratios with only one station, *Bull. seism. Soc. Am.,* **83,** 1574–1594.

Lyu, J., Wang, X.S., Su, J.R., Pan, L.S., Li, Z., Yi, L.W., Zeng, X.F. & Deng, H., 2013. Hypocentral location and source mechanism of the M_S 7.0 Lushan earthquake sequence, *Chin. J. Geophys.,* **56,** 1753–1763. (in Chinese)

Mandal, P. & Dutta, U., 2011. Estimation of earthquake source parameters in the Kachchh seismic zone, Gujarat, India, from strong-motion network data using a generalized inversion technique, *Bull. seism. Soc. Am.,* **101**(4), 1719–1732.

Matsunami, K., Zhang, W.B., Irikura, K. & Xie, L.L., 2003. Estimation of seismic site response in the Tangshan area, China, using deep underground records, *Bull. seism. Soc. Am.,* **93,** 1065–1078.

McCann, M.W.J., 1979. Determining strong motion duration of earthquakes, *Bull. seism. Soc. Am.,* **69**(4), 1253–1265.

Menke, W., 1989. *Geophysical data analysis: discrete inverse theory, Vol. 45, International Geophysics Series,* pp. 289, eds Dmowska, R. & Holton, J. R., Academic Press.

Moya, A. & Irikura, K., 2003. Estimation of site effects and Q factor using a reference event, *Bull. seism. Soc. Am.,* **93**(4), 1730–1745.

Oth, A., Bindi, D., Parolai, S. & Giacomo, D.D., 2011. Spectral analysis of K-NET and KiK-net data in Japan, part II: on attenuation characteristics, source spectra, and site responses of borehole and surface stations, *Bull. seism. Soc. Am.,* **101,** 667–687.

Oth, A., Parolai, S., Bindi, D. & Wenzel, F., 2009. Source spectra and site response from *S* waves of intermediate-depth Vrancea, Romania, earthquakes, *Bull. seism. Soc. Am.,* **99,** 235–254.

Papageorgiou, A.S. & Aki, K., 1983. A specific barrier model for the quantitative description of inhomogeneous faulting and the prediction of strong ground motion. I. Description of the model, *Bull. seism. Soc. Am.,* **73**(3), 693–722.

Parolai, S., Bindi, D. & Augliera, P., 2000, Application of the generalized inversion technique (GIT) to a microzonation study: numerical simulations and comparison with different site-estimation techniques, *Bull. seism. Soc. Am.,* **90,** 286–297.

Parolai, S., Bindi, D., Baumbach, M., Grosser, H., Milkereit, C., Karakisa, S. & Zunbul, S., 2004. Comparison of different site response estimation techniques using aftershocks of the 1999 Izmit earthquake, *Bull. seism. Soc. Am.,* **94,** 1096–1108.

Parolai, S. & Richwalski, S.M., 2004. The importance of converted waves in comparing H/V and RSM site responses estimates, *Bull. seism. Soc. Am.,* **94,** 304–313.

Ren, Y.F., Wen, R.Z., Yamanaka, H. & Kashima, T., 2013. Site effects by generalized inversion technique using strong motion recordings of the 2008 Wenchuan earthquake, *Earthq. Eng. Eng. Vibration,* **12,** 165–184.

Ren, Y.F., Zhou, Y., Wang, H.W. & Wen, R.Z., 2018. Source characteristics, site effects, and path attenuation from spectral analysis of strong-motion recordings in the 2016 Kaikōura earthquake sequence, *Bull. seism. Soc. Am.,* **108**(3B), 1757–1773.

Sadeghi-Bagherabadi, A., Sobouti, F., Pachhai, S. & Aoudia, A., 2020. Estimation of geometrical spreading, quality factor and kappa in the Zagros region, *Soil Dyn. Earthq. Eng.,* **133,** 106110. doi: 10.1016/j.soildyn.2020.106110

Sakhaei, S.R., Mahood, M., Heidari, R. & Arian, M., 2022. Determination of source, site, and path effects of $M_w = 7.3$, 2017 Sarpol-e Zahab using a non-parametric generalized inversion technique, *Pure appl. Geophys.,* **179,** 69–81.

Salazar, W., Sardina, V. & de, Cortina, J., 2007. A hybrid inversion technique for the evaluation of source, path, and site effects employing *S*-wave spectra for subduction and upper-crustal earthquakes in El Salvador, *Bull. seism. Soc. Am.,* **97**(1B), 208–221.

Shoji, Y. & Kamiyama, M., 2002. Estimation of local site effects by a generalized inversion scheme using observed records of 'Small-Titan,', *Soil Dyn. Earthq. Eng.,* **22**(9-12), 855–864.

Toni, M., 2017. Simulation of strong ground motion parameters of the 1 June 2013 Gulf of Suez earthquake, Egypt, *NRIAG J. Astron. Geophys.,* **6**(1), 30–40.

Tsai, C.C.P. & Chen, K.C., 2000. A model for the high-cut process of strong-motion accelerations in terms of distance, magnitude, and site condition: an example from the SMART 1 array, Lotung, Taiwan, *Bull. seism. Soc. Am.,* **90**(6), 1535–1542.

Wang, H.W., Ren, Y.F. & Wen, R.Z., 2017. Research progress of generalized inversion technique used for separating source, path and site effect from ground motions, *Progr. Geophys.,* **32**(1), 78–86.

Wang, H.W., Ren, Y.F. & Wen, R.Z., 2018. Source parameters, path attenuation and site effects from strong-motion recordings of the Wenchuan aftershocks (2008-2013) using a non-parametric generalized inversion technique, *Geophys. J. Int.,* **212,** 872–890.

Wang, H.W., Ren, Y.F., Wen, R.Z. & Xu, P.B., 2019. Breakdown of earthquake self-similar scaling and source rupture directivity in the 2016-2017 central Italy seismic sequence, *J. geophys. Res.: Solid Earth,* **124**(4), 3898–3917.

Wang, H.W. & Wen, R.Z., 2020. Earthquake source characteristics and *S*-wave propagation attenuation in the junction of the northwest Tarim basin and Kepingtage Fold-and-Thrust zone, *Front. Earth Sci.,* **8,** 567939. doi: 10.3389/feart.2020.567939

Wang, S.Y., Wang, J., Yu, Y.X., Wu, Q., Gao, A.J. & Gao., M.T., 2010. The empirical relation between M_L and M_S based on bulletin of seismological observations of Chinese stations, *Earthq. Res. China,* **26,** 14–22.

Wessel, P., Smith, W.H.F., Scharroo, R., Luis, J.F. & Wobbe, F., 2013, Generic Mapping Tools: improved version released, *EOS, Trans. Am. geophys. Un.,* **94,** 409–410. doi: 10.1002/2013EO450001

Xu, Y., Herrmann, R.B. & Koper, K.D., 2010, Source parameters of regional small-to-moderate earthquakes in the Yunnan-Sichuan region of China, *Bull. seism. Soc. Am.,* **100,** 2518–2531. doi: 10.1785/0120090195

Zafarani, H., Hassani, B. & Ansari, A., 2012. Estimation of earthquake parameters in the Alborz seismin zone, Iran using generalized inversion method, *Soil Dyn. Earthq. Eng.,* **42,** 197–218.

Zhang, L.B., Fu, L., Liu, A.W. & Chen, S., 2023. Simulating the strong ground motion of the 2022 M_S 6.8 Luding earthquake, Sichuan, China, *Earthq. Sci.,* **36**(4), 283–296.

Zhang, Y.J., Qiao, H.Z., Cheng, W.Z. & Liu, J., 2017. Attenuation characteristics of the media in Sichuan basin region, *J. Seismol. Res.,* **30**(1), 43–48 (in Chinese)

Zhao, C.P., Chen, Z.L., Hua, W., Wang, Q.C., Li, Z.X. & Zheng, S.H., 2011. Study on source parameters of small to moderate earthquakes in the main seismic active regions, China mainland, *Chin. J. Geophys.,* **54,** 1478–1489. (in Chinese)

Zhou, Y., Wang, H.W., Wen, R.Z., Miao, T.M. & Cui, J.W., 2022. Source characteristics and path attenuation for the Yangbi, China seismic sequence in 2021, *Pure appl. Geophys.,* **179,** 2721–2733.